Spring 2017

Experimental and Theoretical Study of Vapor Phase Species above Hot Rocky Exoplanet Analogues

Michal Bulak

EXPERIMENTAL AND THEORETICAL STUDY OF VAPOR PHASE SPECIES ABOVE HOT ROCKY EXOPLANET ANALOGUES

A Masters Thesis

Presented to

The Graduate College of

Missouri State University

In Partial Fulfillment

Of the Requirements for the Degree

Master of Science, Materials Science

By

Michal Bulak

May, 2017

EXPERIMENTAL AND THEORETICAL STUDY OF VAPOR PHASE SPECIES ABOVE HOT ROCKY EXOPLANET ANALOGUES

Physics, Astronomy and Materials Science

Missouri State University, May, 2017

Master of Science

Michal Bulak

ABSTRACT

With the James Webb Space Telescope and other space-based missions launching in the next few years, the astrophysics community awaits an exciting time. This work is an answer to a call for the laboratory contributions necessary to analyze the data of unprecedented accuracy. I performed a laboratory analysis of an analogue of a hot super earth atmosphere. This type of an extra solar planet has a rocky composition and has extremely high temperature (from 1500˚C – 5000˚C). I performed infrared spectroscopy on the gas phase vapor above a mixture of two binary systems: SiO_2 with Al_2O_3 and CaO with SiO_2. They are simplified systems that are representations of atmospheres of exoplanets of the specified type. The results are the identification of gaseous AlOSi – a radical that is possibly a constituent of an atmosphere along with an estimate of its opaqueness; first identification of three infrared lines of gaseous $CaSiO_3$ – a salt that has not had an experimental infrared characterization. I hope these findings will aid the modelling of hot rocky planet's atmospheres.

KEYWORDS: infrared spectroscopy, hot rocky exoplanets, atmosphere, adduct, radical, aluminum silicate, calcium silicate

This abstract is approved as to form and content

_____

David Cornelison, PhD
Chairperson, Advisory Committee
Missouri State University

EXPERIMENTAL AND THEORETICAL STUDY OF VAPOR PHASE SPECIES ABOVE HOT ROCKY EXOPLANET ANALOGUES

By

Michal Bulak

A Masters Thesis
Submitted to the Graduate College
Of Missouri State University
In Partial Fulfillment of the Requirements
For the Degree of Master of Science, Materials Science

May, 2017

Approved:

_____
David Cornelison, PhD

_____
Ridwan Sakidja, PhD

_____
Kartik Ghosh, PhD

_____
Julie Masterson, PhD: Dean, Graduate College

ACKNOWLEDGEMENTS

I want to express gratitude to my parents: if it were not for you, I would not be where I am now – dziękuje. I also want to thank Dr. Cornelison for challenging me, and at the same time, providing scientific and moral support that got me through the Masters Program.

I dedicate this thesis to all graduate students. Let us hope hard work pays off.

TABLE OF CONTENTS

LIST OF TABLES

LIST OF FIGURES

INTRODUCTION

Over 2000 years ago, Epicurus, one of the major philosophers in the Hellenistic period, said, “There are infinite worlds both like and unlike this world of ours.” (Toomer 1984). It is now known that the observable Universe has billions of galaxies both like and unlike our own galaxy - the Milky Way. Each of these galaxies encompasses billions of stars, such as our Sun. Often, there are planets orbiting these stars. It is a misnomer to simply label these as planets, though. Rather, they are interchangeably called exoplanets or extrasolar planets. Conventionally, planets have three well-defined characteristics. According to the International Astronomical Union, a planet is an object that orbits the Sun, is massive enough for its own gravity to make it nearly spherical, and has cleared its orbit of debris. The definition of an exoplanet includes two of the three mentioned conditions while excluding the parameter that it orbits the Sun. In fact, an exoplanet orbits any star other than the Sun.

There has been an extensive amount of research into exoplanets by scientific communities around the world. This research has consumed vast amounts of money and resources with the intention of further understanding our universe. Various studies previously conduced have revealed much about the scale and diversity of exoplanets, many having existed well before the human species emerged on Earth. Exploring the unknown is often conjectured to be a fundamental part of human nature. This innate drive is exactly what helps scientists begin to answer questions, such as: how did the universe begin? Because processes such as star formation and migration take millions of years, it is not possible for humans to study their changes by direct observation. Nevertheless,

astronomers can produce theories, which describe the mechanisms that govern these processes, allowing them to model and predict the past and future of both stars and planets.

An example of an impact that a discovery in the field of exoplanets can make, is the detection of the first exoplanet, 51 Pegasi b, in 1995 (Mayor and Queloz 1995). Until then, astronomers could see no way for a planet to be as massive as a half of the Jupiter's mass and orbit a star in only 4 days. Additionally, some of the well-known theories, including the nebular theory explaining how the Solar System formed, were challenged. A detection of a hot gas giant planet HD 209458b, orbiting close to its star, put the theory of formation in doubt and changed the way I perceive the Solar System and the Universe (Charbonneau et al. 2000; Henry et al. 1999, 2000). As Bruce Macintosh from Stanford University said: "There has never been a moment when theory has caught up with observations" (Clery 2016). The vast divergence of findings gives researchers a great amount of motivation to further explore the Universe and hope to understand it better.

Observational Techniques

There are three major techniques used for detection and characterization of exoplanets: radial velocity method, astrometry (microlensing), and transit method (photometry). The first method is based on the analysis of a small, systematic Doppler shift in wavelength of multiple absorption lines that create a star's spectrum. Christian Doppler first discovered the Doppler shift in 1842. It describes the change between the observed and emitted wavelength, when either the source or the receiver is in motion. During the star's motion around the star-planet barycenter, radial component of the stellar

velocity changes, which indirectly leads to a detection of the planet orbiting the star. Equation 1 represents an expression for the relativistic Doppler shift in the observer's reference frame. λ_{obs} and λ_{em} are observed and emitted wavelengths and $\beta = (v/c)$, where v is the relative velocity between the source and the receiver at an angle θ with respect to the direction from the observer to the source. C is the speed of light (Lang 1980).

$$\lambda_{obs} = \lambda_{em} \frac{(1+\beta\cos\theta)}{\sqrt{(1-\beta^2)}} \quad (1)$$

Combining the expression above with Kepler's third law of planetary motion, it is possible to determine the star-planet distance, orbital period and an estimate of planet's mass. One of the main limitations of this method is that it can only measure movement along our line-of-sight. If the planet's orbital plane is not lined up with the line-of-sight of the observer, the velocity measurement will only be a component of the true velocity. Consequently, the calculated mass will be smaller than the true mass of the planet (I can only calculate the upper limit for the mass of the planet). Astrometry, which will be discussed further, is used to correct for this effect.

The first major exoplanet discovery using the radial velocity method was planet 51 Peg b orbiting the 51 Peg star. The planet has a 4-day period, and mass of at least 0.47 M_J (Mayor and Queloz 1995). Radial velocity is a difficult but very effective method for exoplanet detection. According to the NASA Exoplanet archive, as of April 2016, radial velocity method facilitated a discovery of 596 extrasolar planets.

Astrometry is the oldest method of detecting extrasolar planets and its history goes back to Hipparchus in 190 BC (G.J. Toomer 1984). This field of astronomy is based

on the measurements of positions, movements and magnitudes of stars in the Universe. In the context of exoplanet detection, precise, continuous astrometry allows to determine transverse component of the displacement of the star due to the gravitational perturbation of a planetary orbital motion. When the observations are done from Earth, their accuracy is largely restricted by Earth's atmosphere. Astrometry measurements are usually done using an interferometer but in case of the most advanced astrometry space mission so far – Gaia (launched in 2013 by ESA, European Space Agency) – imaging telescopes were utilized. According to the Agency (Year), Gaia "will provide detailed information (accuracy of approximately 20 μas) on stellar evolution and star formation in our Galaxy. It will clarify the origin and formation history of our Galaxy." Figure 1 is Gaia's first sky map that was created and annotated based on its first 14 months of operation.

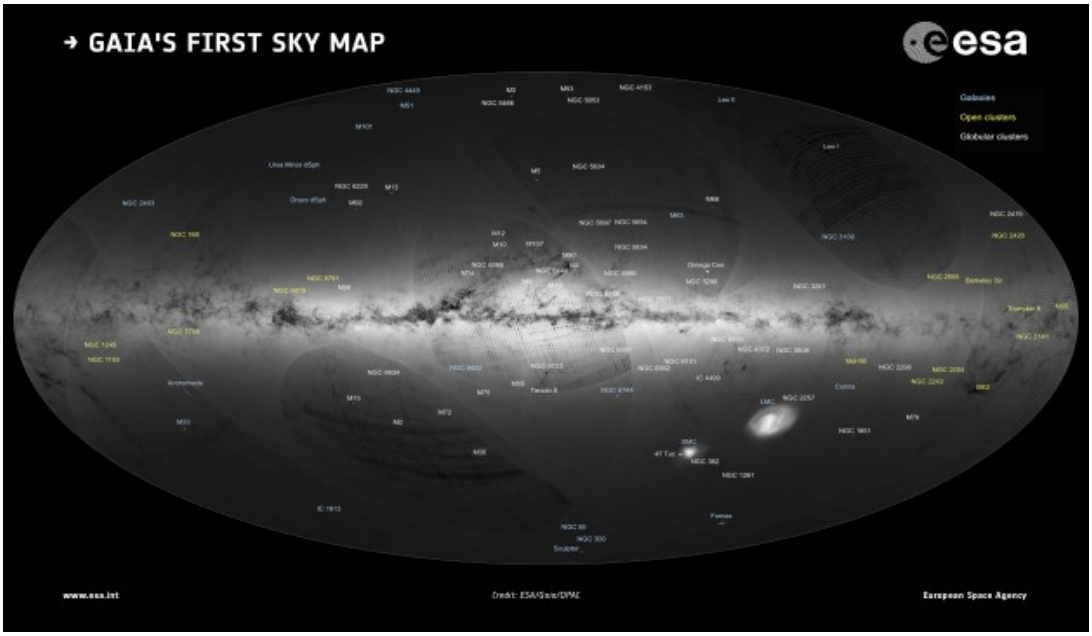

Figure 1. Gaia's first sky map published by ESA on September 14, 2016 (Copyright: ESA/Gaia/DPAC).

Further objectives of the mission include unprecedented accuracy measurements of: the

star and planet motions, inclinations of the orbital planes, distances between stars and true planet masses. On September 13, 2016, the first catalogue of more than a billion stars from ESA's Gaia satellite was published.

Astrometry as a method of exoplanet detection has a few limitations. The most important one concerns the star-to-planet mass ratio. The planet needs to be massive enough to significantly affect the trajectory of the star (technology so far allows detection of Jupiter-size planets). The accuracy of the measurements depends also on the distance of the examined object from the Earth. A displacement of a body that is closer would appear as greater in amplitude, compared to a body that is further away. Hence, the further away the body is, the less accurate astrometry is.

Transit photometry is a different method of exoplanet detection that has been on the rise for the past 20 years. Planets, whose orbits cause them to transit a stellar disk, can be detected by monitoring the stellar flux for periodic dips (Armitage, 2010). A transit is described by a smaller celestial body (a planet) moving in front of the larger (a star). Figure 2 highlights key stages of a planet orbiting a star from the observer's perspective and the corresponding light curve.

Analysis of the light curve shows two dips in the flux. A greater dip corresponds to the transit when the planet blocking a fraction of the star light reduces the intensity of the light. Measurement of the dip gives a planet-to-star area ratio. The second drop in intensity appears when the planet goes behind the star. The dayside flux of the planet is a resultant of subtracting the flux during the secondary eclipse from the flux of both the star and the planet (just before the secondary eclipse). Infrared photometry of the

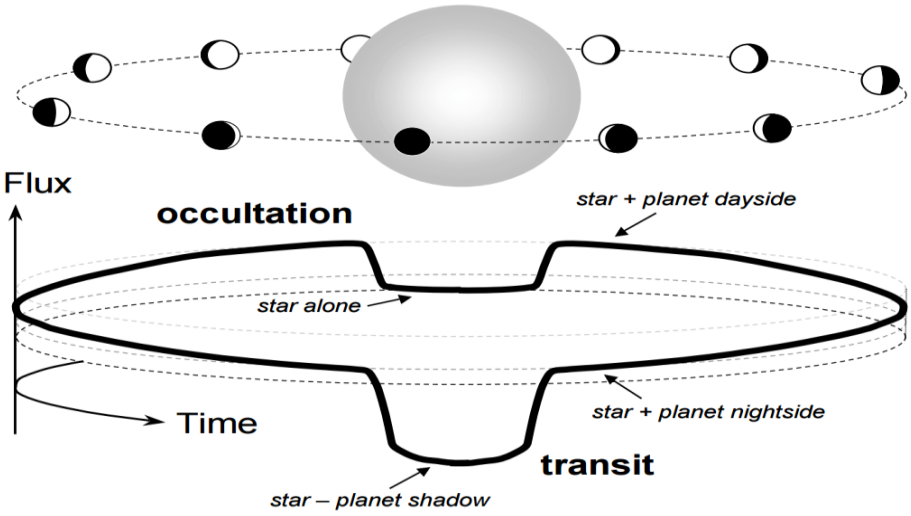

Figure 2. A planet transiting a star and its corresponding light curve (Winn 2010).

secondary eclipse allows estimating the planet's temperature with respect to the star's temperature. In 2003, a Harvard professor – Charbonneau – used the following formula (Equation 2) to estimate the depth (ΔF) of the secondary eclipse (Charbonneau, 2003).

$$\Delta F \cong \frac{T_P}{T_s}\left(\frac{R_p}{R_s}\right)^2 \qquad (2)$$

T_p, T_s, R_p,and R_s are respectively star's and planet's temperatures and their radii.

The first detection of a transiting extrasolar planet, HD 209458b (Charbonneau et al. 2000; Henry et al. 1999, 2000) was an anticipated breakthrough that began a new period of significant discoveries in research area of extrasolar planets. During the detection of HD 209458b, the Space Telescope Imaging Spectrograph on board of the Hubble Hubble Space Telescope registered a drop of about 1.5% for HD209458b (Charbonneau et al. 2000).

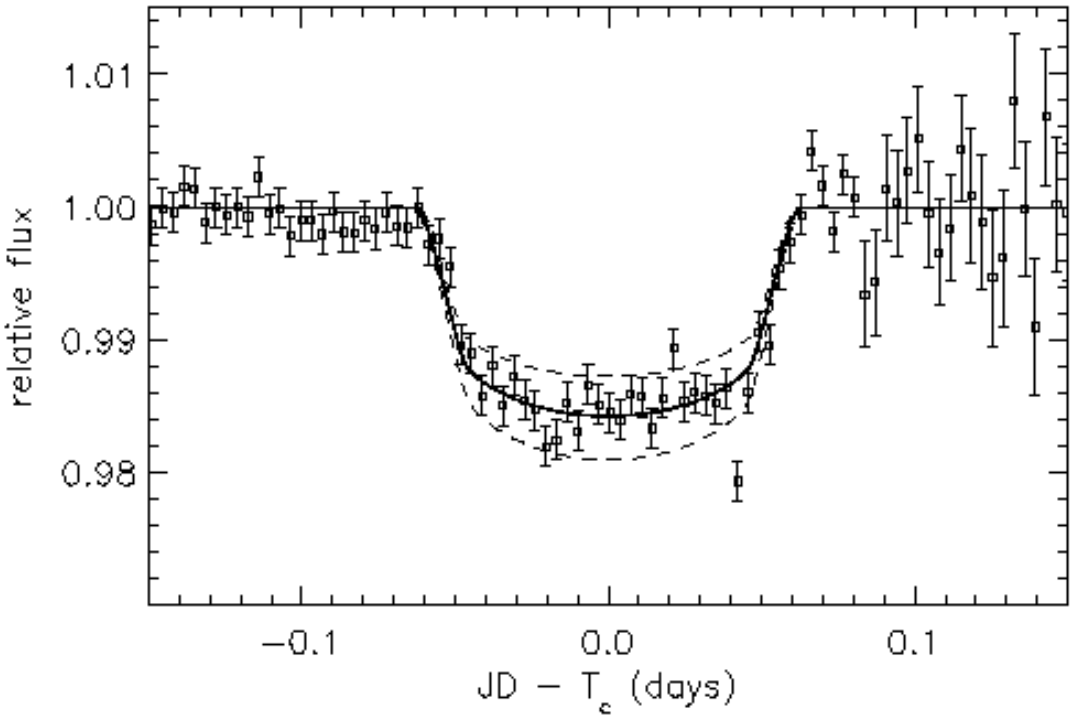

Figure 3. Curve light of HD 209458b that confirmed its detection (Charbonneau et al. 2000).

Planet orbits its star at 9 stellar radii every 3.5 days and creates a 2.5 hour transit observation time (Henry et al. 2000; Charbonneau et al. 2000).

Transiting photometry has one major limitation. Astronomers can only use this method to observe planets whose orbits line up with the line-of-sight of the observer. Probability for these conditions to occur is related to the ratio of star's radius to the orbit's radius (in case of small stars, also dependent on planet's ratio). To give an idea of how unlikely it is, there is only 0.47% chances that a planet orbiting the Sun, such as Earth, will randomly align producing a detectable transit. Nevertheless, ground-based missions (MEarth Project, SuperWasp) and space-based missions (COROT and Kepler) detected thousands of exoplanets by scanning the skies.

Diversity of Exoplanets

Thus far, 3533 extra solar planets have been discovered by multiple methods (nasa.gov 2016). Exoplanets vary widely and can be categorized by a few different parameters including: mass, orbit, temperature, and composition. The masses of exoplanets range from 0.02 M_E for PSR B1257+12 A (Earth's mass units), (Wolszczan 1994) to 28.5 ± 1.9 M_J for DENIS-P J082303.1-491201 (Jupiter's mass is 318 times greater than M_E), (Sahlmann et al. 2013). Orbital periods cover a wide spectrum with the longest at around 1 million years of 2MASS J2126-8140 (Cruz et al. 2009) and the shortest at around 2.2 hours (PSR J1719-1438 b, Bailes et al. 2011). However, most planets fall somewhere in the middle between these limits. Figure 4 shows a mass-period distribution with color-coded method of detection of confirmed exoplanets (nasa.gov 2016).

The temperature of the exoplanets is closely related to its distance from the star, mass and density. It is determined by analyzing a drop in the stellar flux drop during the occultation stage. Approximation of the temperature is determined with the assumption that a planet radiates like a perfectly black body. Planet's equilibrium temperature (T_P) is calculated using Equation 3:

$$T_p = T_s \left(\frac{(1 - A) R_S^2}{4a^2} \right)^{\frac{1}{4}} \quad (3)$$

R_S and T_S are star's radius and effective temperature, A and a are the planet's Bond albedo and semi-major axis. The first temperature measurements were done using the

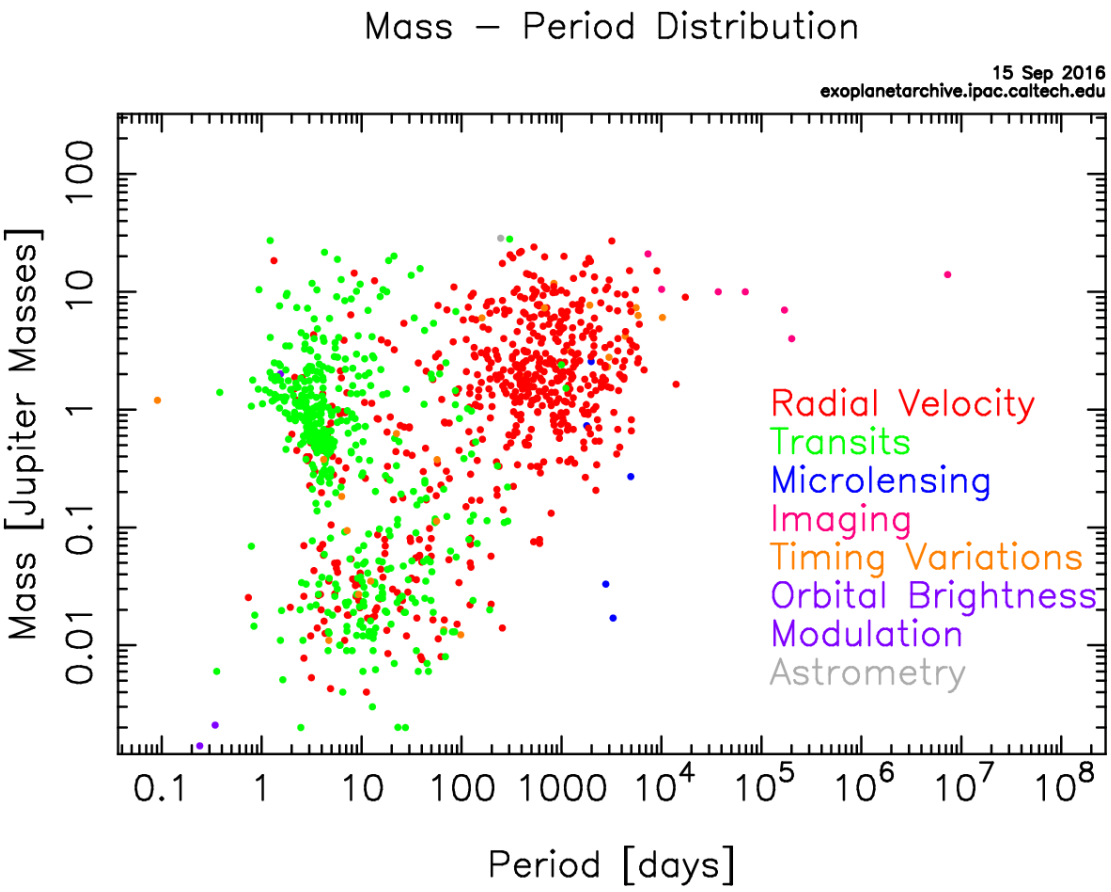

Figure 4. Mass versus period distribution of exoplanets detected as of September 2016 (exoplanetarchive.ipac.caltech.edu).

data from Spitzer Space Telescope by Deming et al. on planet HD 209458b (Deming et al. 2005) and Charbonneau et al. on TrES-1 (Charbonneau et al. 2005). Temperatures, like other parameters of exoplanets, vary immensely: from the minimum of 50 K all the way to 7143 K (exoplanets.eu).The radii of the exoplanets are determined by the analysis of the drop in the intensity during the transit. The drop is proportional to the ratio of the squares of planet's radius to star's radius. Figure 5 shows a distribution of radii vs. calculated temperature data available for 210 exoplanets (exoplanets.eu 2017). Out of over 3,500 discovered exoplanets, only 28 have a measured temperature and plot has a similar distribution of temperatures to the one above.

Enormous ranges in volume, mass and temperature lead to a variety of different densities. Based on the mean density researchers attempt to infer a general type of planet's internal structure. Despite similar densities, there are vast degeneracies in bulk composition. Composition models predict types from mini-Neptune (thick H/He layer) to Earth-like rocky planets (silicates with heavy molecules atmosphere) to Water Worlds with high water content (Fortney et al. 2007; Seager et al. 2007). The complex composition models were created combining multiple known parameters and under many assumptions. Models include molecules that are common in the solar system (iron, rock. Ices, H/He gas) and were constrained by the probability of occurance of certain constituents (thermal equilibrium calculations) as well as known external and internal conditions of the planet.

Atmospheres of Exoplanets

Knowledge of the planet's atmosphere significantly mitigates the degeneracies in

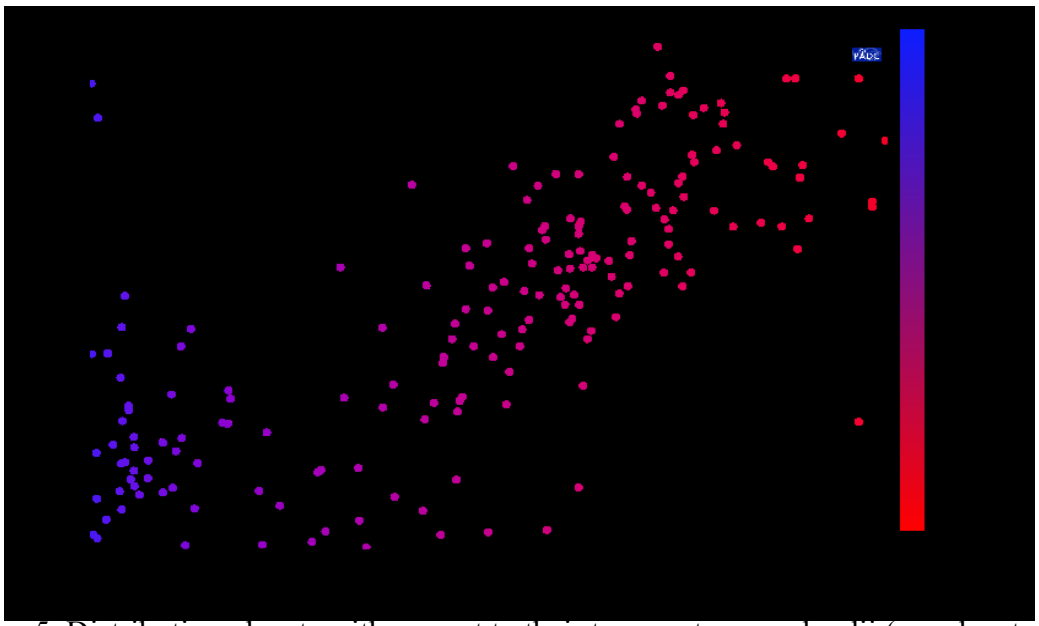

Figure 5. Distribution planets with respect to their temperatures and radii (exoplanet.eu).

the bulk composition. Characterization of an atmosphere includes indicating abundances of its constituents, relative pressures and temperatures. Additionally, atmospheres can have a cloud structure and a wind pattern. All of the factors above play a key role in characterization of the atmosphere.

First atmosphere detection was of a Hot Jupiter HD 209458b with the Hubble Space Telescope (HST) data (Charbonneau et al. 2002). The detection was possible due to favorable transit observation conditions: planet's orbit almost perfectly lines up with the line-of-sight from HST, it is close to the star (<=0.05AU) and has high temperature (1000 – 2000K). As the light reflected from the star goes through the planet's atmosphere, molecules leave unique absorption features on the light curve, which allowed the identification of the gas constituents. Modeling of a cloud structure (Ackerman and Marley 2001) and calculation of transmission spectra (Seager and Sasselov 2000; Hubbard et al. 2001) also played a significant role in atmosphere's detection. As the atmosphere observation of an exoplanet requires extreme precision, it can be only performed by space-based spectrometers such as one on HST or Spitzer Space Telescope. So far, the spectroscopic analysis of only the gas giants' light curves, have produced characterizations of the atmospheres (among others: Deming et al. 2005; Knutson et al. 2008; Swain et al. 2008; Charbonneau et al. 2002).

Modeling of the atmosphere is of critical importance to the analysis of the observed spectra. Computed atmosphere model is based on the radiative transfer equation 4, which relates the change in a beam of intensity dI/dz to losses from the beam $-\kappa I$ and gains to the beam ε. Radiative transfer equation in 1D takes the form of

$$\mu \frac{dI(z,v,\mu,t)}{dz} = -\kappa(z,v,t)I(z,v,\mu,t) + \varepsilon(z,v,\mu,t) \quad (4)$$

Where I [$Jm^{-2}s^{-1}Hz^{-1}$] is the intensity of a photon beam, κ is the absorption coefficient (takes into account absorption and scattering out of the radiation beam); ε is the emission coefficient; μ = cosθ, where θ is the angle away from surface normal and z is vertical altitude that has a specified temperature and pressure. Absorption and emission coefficients, κ and ε, have built-in opacity, chemistry and clouds dependencies. For a single gas species, the absorption coefficient is represented by equation 5:

$$\kappa(\lambda,T,P) = n(T,P)\sigma(\lambda,T,P) \quad (5)$$

Where n is the gas number density and σ(λ,T,P) is the cross section summed over all molecular lines that contribute at a given wavelength λ. Gas number densities can be calculated from equilibrium chemistry (Lodders and Fegley 2002). The cross-section measurements can be achieved from laboratory measurements. The existence of clouds introduces a high opacity of solid materials therefore making the radiative transfer more complex (Sanchez-Levega 2004; Perez-Hoyos and Hueso 2004).

Deming and Seager in exoplanet atmosphere review in 2010 suggested dividing atmospheres of exoplanets into 5 categories:

1. Atmospheres dominated by volatile gases H and He in proportions similar to cosmic. The gases come from either protoplanetary nebula (explain) or from planet formation from the gravitational collapse. Typical planets that have this atmosphere are giants and ice giants.

2. Atmosphere is a mixture of hydrogen in the form of H_2 and outgassing of the planet. The abundances of the elements depend on the original composition of

planetesimals that created the planet (Elkins-Tanton and Seager 2008; Schaefer Fegley 2010). Typical planets with this type of an atmosphere are rocky, have a mass of 10-30 M_E and have a low temperature that allows them to keep the hydrogen in planets' atmospheres. These atmospheres do not have He, as rock does not have the ability to preserve He.

3. Atmospheres that are a mixture of outgassing of the planet's constituents (therefore components depend on the planet's composition) and CO_2. This category is characteristic for planets that are not massive enough to keep H or He in their atmospheres and warm enough to evaporate CO_2 (e.g. Earth). If H_2O signatures are found, the planet might have liquid water oceans.

4. Atmospheres of hot super Earths with temperatures greater than 1500 K. Because of the high temperatures, atmospheres do not contain any volatiles (H, He, C, N, O, S). Instead, atmospheres are made up from silicates enriched in refractory metals such as Ca, Al or Ti (Schaefer and Fegley 2009).

5. The last category is planets that have a negligible exosphere or have completely lost their atmospheres. This type of planets could be identified by a substellar point hotspot, which is (Seager and Deming 2009). Mercury is an example of a planet of this category that can be found in the Solar system.

Up to this date, hot Jupiters' atmospheres are the only type of extrasolar atmosphere studied observationally. However, the James Webb Space Telescope (JWST) mission launching in 2018 is expected to produce spectrographic data with precision sufficient to analyze the atmospheres of other types of exoplanets. Before the JWST data can be fitted, spectral analysis models need to be created and tested.

Up to date, based on the lack of complete chemical and physical data, a great challenge for the scientific community will be besides the data acquisition: its analysis. A white paper by J. Fortney et al. was published in 2016 summarizing a large gap in physical and chemical contributions that can be facilitated via laboratory or ab initio methods (Fortney et al. 2016). Keeping in mind the upcoming missions (JWST and others), it is critical to be as prepared as possible to analyze the information from JWST before the raw data gets to the community of researchers.

Among the atmospheric types mentioned above, atmospheres of hot super Earths are of special interest to us. The super Earths orbit their stars close enough to be heated by irradiation to extremely high temperatures (above 1500 K). There are no equivalents of planets of this type in the Solar System. Based on a study of mass-radius relationship, for planets with a mass ranging from 1-100 Earth-mass, one could determine a general composition of a planet of this type to be dominated by komatiite materials (Grasset, 2009). That means that the most abundant species in the planets' atmospheres are: SiO_2, MgO, Al_2O_3, TiO2, Fe_2O_3, CaO, Na_2O (Schaefer and Fegley 2004). Knowing the temperature of the planet, its main constituents, and the fact that its atmosphere is created by outgassing, it is possible to try and imitate the atmospheric conditions from the planet in a lab setting as well as by thermodynamical calculations.

Modeling of such atmospheres has been already done using the MAGMA code (Lodders and Fegley 2004). However, when performing laboratory experiments on systems of chosen species among the komatiite constituents - additional results have been produced that have not been included in the calculations. In order for the calculations to be complete, one needs to know what species will be present in both liquid and gas phase as well as their thermodynamical data such as heat capacity, Gibbs free energy and entropy. In this work, a laboratory investigation of two binary systems have been conducted: mixture of SiO_2 and Al_2O_3 as well as SiO_2 and CaO. During both experiments new species were created that exist only in the gas phase and are characterized as adducts.

My long term goal is to be able to identify the spectral features representing the adducts and calculate their thermodynamical data needed as input for codes like

MAGMA. Hopefully in the future, given the JWST spectrographic data, my results will aid identification of gas phase species that make up an atmosphere along with their vapor pressures at a given temperature.

THEORY

An exoplanet is dubbed a hot super Earth if its mass is 1 to 10 times the Earth's mass and its temperature is above 1500K. These extreme conditions indicate/suggest that the atmosphere of the planet is made up of evaporates of the planets' constituents. The composition of the planet is inferred from its density. However, a single density value can be a result of different compositions. As the densities range from 0.71 to 10.4 g cm^{-3}, multiple combinations of species could end up within that range. It has been demonstrated for GJ 1214 b that the observation of the atmosphere could help determine the bulk composition of the planet itself (Miller-Ricci & Fortney 2010). However to make successful observations of the atmospheres, it is key to have models predicting possible and easily identifiable spectral traces that could indicate the planet's composition.

The continental crust and the bulk silicate Earth are good representations of hot rocky exoplanets and their compositions are shown in Table 1 (Schaefer et al. 2012). Assuming melt-vapor, and vapor equilibria, it is possible to compute the abundances of gas phase species in a form of vapor pressures of the planet's constituents. Given a set of thermodynamic data for a number of melt and vapor species as input, Fegley and Cameron developed the MAGMA code that outputs a vapor composition that is an equivalent of an atmosphere of a hot super earth. It is a rapid mass-balance, mass action algorithm that takes under consideration competing chemical reactions for multiple molecules at the same time. The basis for the method is a complete set of

thermodynamical data for melt and vapor species that take part in the chemical reactions.

Table 1. The weight percent compositions representing the hot super Earths and bulk compositions of vaporizing planets (Wedepohl 1995; Kargel and Lewis 1993).

Element	Continental Crust (wt. %)	Bulk Silicate Earth (wt. %)
O	47.20	44.42
Si	28.80	21.61
Al	7.96	2.12
Fe	4.32	6.27
Ca	3.85	2.46
Na	2.36	0.29
Mg	2.20	22.01
K	2.14	0.02
Ti	0.401	0.12
P	0.076	0.008
Cr	0.013	0.29
Mn	0.072	0.11
H	0.045	0.006
C	0.199	0.006
N	0.006	0.88x10-4
S	0.070	0.027
F	0.053	0.002
Cl	0.047	0.004

The calculations have been done for multiple planets including CoRoT-7 b (Schaefer et al. 2012). The gas phase species and their abundances for CoRot 7-b atmosphere are shown in Figure 6. For that calculation at 2500 K and the pressure of 10^{-2} bars, two different planetary compositions were considered: the continental crust and the Bulk Silicate Earth (species above 0.1% mole fraction are shown).

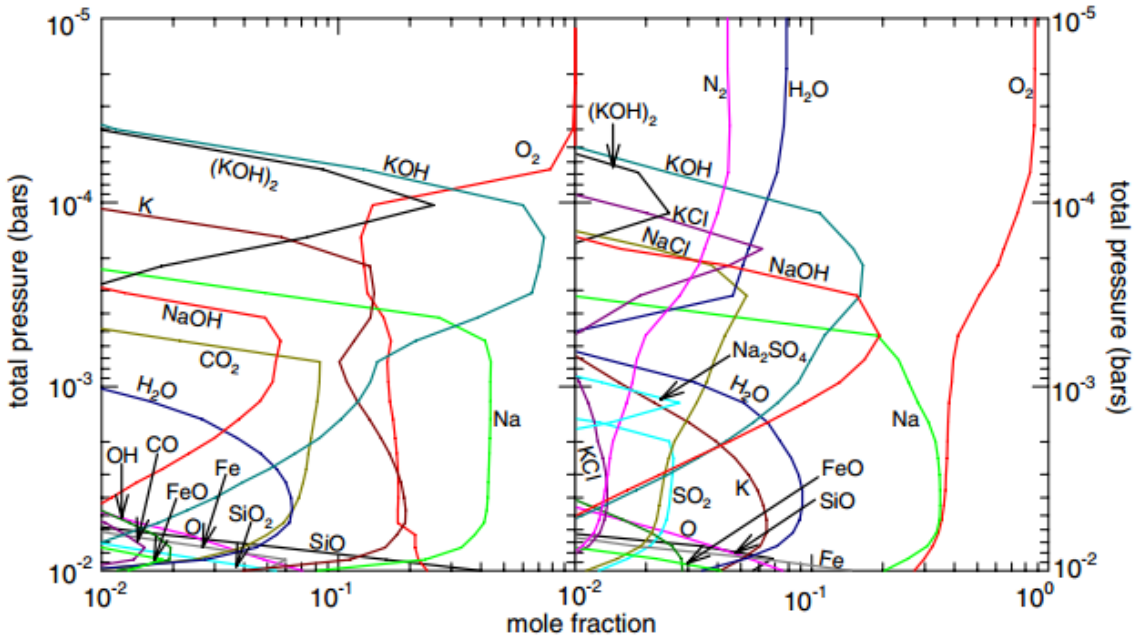

Figure 6. Calculated atmospheric makeup of a planet similar to CoRoT-7b for komatiite (left) and BSE compositions (right) (Schaefer et al. 2012).

Miguel et al. (2011) performed similar calculations for 193 planetary candidates detected by the Kepler mission. Table 2 shows the initial compositions used for the calculations and Figure 7 illustrates the resulting atmospheric compositions of planets as a function of planet's surface temperature. The distance between the planet and the host star was found to be a key factor in determination of a planet's atmosphere.

Table 2. Initial compositions (Wt. oxide %) used for atmospheric calculations (Miguel et al. 2012)

Oxide	SiO_2	MgO	Al_2O_3	TiO_2	Fe_2O_3	FeO	CaO	Na_2O	K_2O
Komatiite	47.10	29.60	4.04	0.24	12.80	0.0	5.44	0.46	0.09
BSE	45.97	36.66	4.77	0.18	0.0	8.24	3.78	0.35	0.04

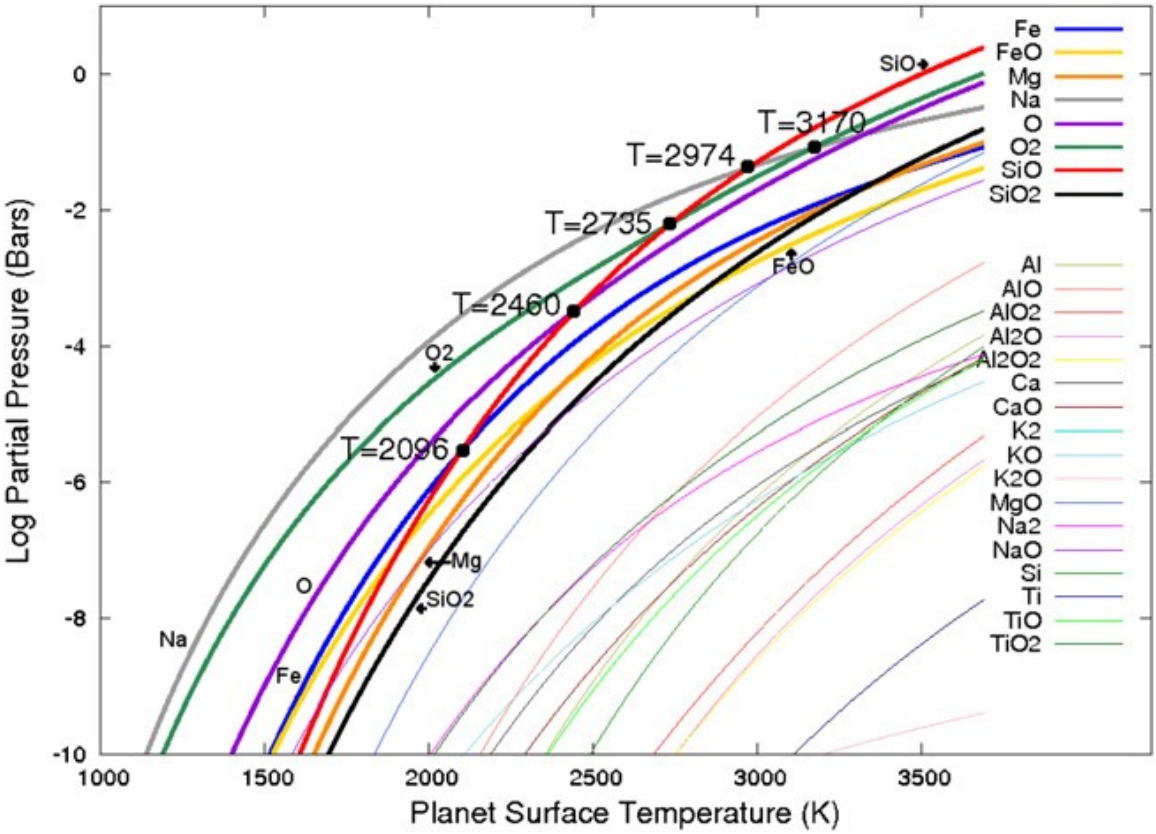

Figure 7. Partial pressures of atmospheric constituents for komatiite composition of a planet (Miguel et al. (2011).

Knowing the constituents of the planet, the hot super Earths' atmospheres could be recreated in the lab setting by the following process: heating up the constituents of the planet to the desired temperature value, and after reaching an equilibrium, analyzing and quantifying the gas phase species that were created. Taking under consideration the complexity of the analysis of multiple species at the same time, in order to thoroughly investigate all feasible combinations of the evaporated species, I started with the most basic case of a planet made up of only one species (following the komatiite wt. oxide % composition) – described in detail by Bosh, Y. and Gemar, H. After I finished analyzing species separately, I moved on to binary systems which is going to be covered in this thesis work. The more complex systems (ternary) will be analyzed in the future.

Phase Diagrams

In order to plot phase diagrams of pure materials, one needs the temperature and the pressure data. To graphically represent phases of a two-compound system (binary), one more variable is needed – composition. The binary phase diagrams are plotted for constant pressure and show the phase as a function of temperature and composition of the system. An applicable binary phase diagrams is shown in Figure 8. Theoretical ground for phase diagrams is thermodynamics first laid out by Gibbs (1906). The phase rule that is represented graphically in a phase diagram is given by equation 6:

$$P + F = C + 2 \tag{6}$$

Where P, F, C are number of phases, number of degrees of freedom, and number of components. For the details of the derivations of these theorems, readers are pointed to the following materials: Findlay (1951), Ricci (1951), Darken and Gurry (1953), or Bowen (1956). The phase diagram CaO-SiO_2 shows all possible solid and liquid phases that are present as a function of temperature and composition of the system. The phase reactions at given temperatures with equivalent liquid compositions of the system are given in Table 3. The phase diagram however, does not include the existing gas phases, which are of great interest to us. It is reasonable to assume that when analyzing the diagram, above the liquid phase of the species, exists a gaseous phase that has not been indicated. In order to mirror that phase, I start with a sample with a specific ratio of CaO

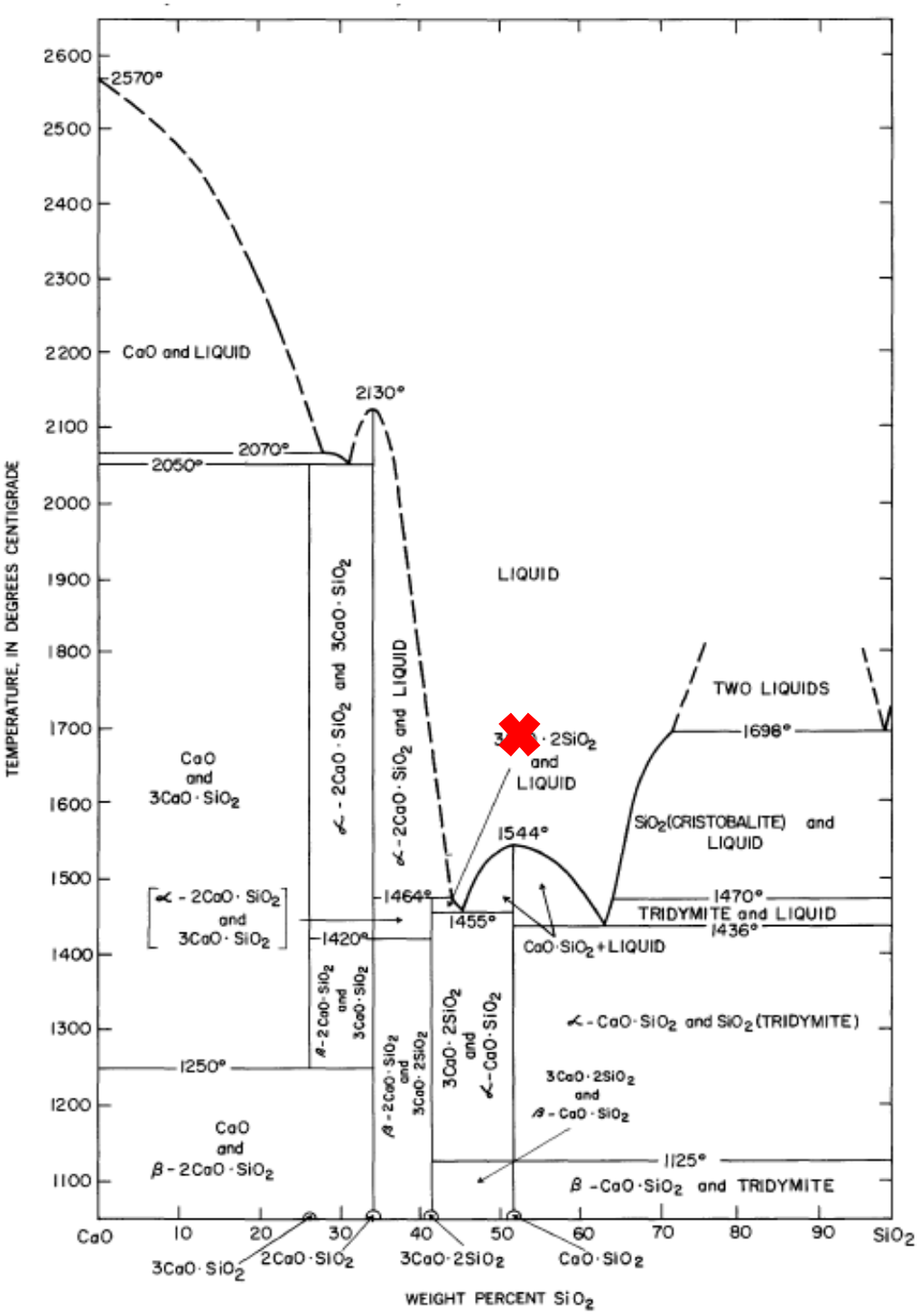

Figure 8. The phase diagram of a binary system CaO - SiO_2 (Morey 1964).

Table 3. Invariant points of the binary system CaO-SiO_2 (Morey 1964).

Phase reaction	Temperature (˚C)	Combination of liquid (% by weight) CaO – SiO_2
$3CaO * SiO_2 \Leftrightarrow CaO + L$	2070	71.5 - 28.5
$3CaO * SiO_2 \Leftrightarrow CaO + \alpha - 2CaO * SiO_2$	1250	76.75 – 32.25
$3CaO * SiO_2 + \alpha - 2CaO * SiO_2 \Leftrightarrow L$	2050	69.5 – 30.5
$\alpha - 2CaO * SiO_2 \Leftrightarrow L$	2130	65.11 – 34.89
$\alpha - 2CaO * SiO_2 \Leftrightarrow \beta - 2CaO * SiO_2$	1420	No liquid
$3CaO * SiO_2 \Leftrightarrow \gamma - 2CaO * SiO_2$	675	No liquid
$3CaO * 2SiO_2 \Leftrightarrow \alpha - 2CaO * SiO_2 + L$	1464	55.5 – 44.5
$3CaO * 2SiO_2 + \alpha - CaO * SiO_2 \Leftrightarrow L$	1455	54.5 – 45.5
$CaO * SiO_2 \Leftrightarrow L$	1544	48.27 – 51.73
$\alpha - CaO * SiO_2 \Leftrightarrow \beta - CaO * SiO_2$	1125	No liquid
$\alpha - CaO * SiO_2 + SiO_2(\text{tridymite}) \Leftrightarrow L$	1436	36.1 – 63.9

to SiO_2, so that at an achievable for us temperature, it is all in the liquid phase. Then, above the melting temperature, the system starts evaporating. As an example, the powder sample for this system is 48% CaO and 52% SiO_2 (marked by "X") by weight and following the phase diagram, at a temperature above 1544 ˚C it congruently melts, which means that it completely turns into a liquid phase species of its own composition.

The challenge that I are facing is to identify the constituents in the gas phase of the system, above the liquid phase. From the literature review, I know what would be the vapor above pure SiO_2 and pure CaO. However, it has been shown that at a high temperature, when evaporating a melt that is a combination of both, new species appear that exist only in the gaseous phase. Therefore, given the extreme conditions, adducts – complex vapor species that are a result of a combination of two or more entities – can be formed (Hastie 1975). As there is not much data available for adducts, it is a great

motivation for further investigation of complex gas species at high temperatures.

Computational Method

The challenge of identifying the species is approached by two different methods: experimental and computational. The latter is solved by using the Gaussian software package – Ab Initio calculations to generate the infrared vibrational frequencies for all IR active species (Gaussian 09).

The method for these simulations is performing Density Functional Theory calculations of electronic ground state for a geometrically optimized structure. In order to perform the Ab Initio calculations one needs to use the DFT based on theorems by Hohenberg and Kohn. The first theorem says that all properties of the system can be derived from the electron density function – experimentally observable phenomena – including the total energy. The second theorem states that the electron density that minimizes the total energy corresponds to the ground state density. Based on the two theorems and Kohn-Sham theory, DFT methods are practical and accurate in many cases. Table 4 shows the different types of level of theory and their corresponding accuracy (Cramer 2004).

The calculations start with optimizing the geometrical structure of a molecule by finding its minima on the potential energy surface. At those points, the gradient of energy will simply be zero. To do that, both the electron-electron and electron-nucleus interactions are taken into account.

Table 4. Scale factors and RMS errors for infarcted vibrational features calculated using different levels of theory (Cramer 2004).

Level of theory	Scale factor	RMS error (cm^{-1})	Outliers (%)
AM1	0.9532	126	15
PM3	0.9761	159	17
HF/3-21G	0.9085	87	9
HF/6-31G(d)	0.8953	50	2
HF/6-31G(d,p)	0.8992	53	3
HF/6-311G(d)	0.9361	32	
HF/6-311G(d,p)	0.9051	54	3
HF/LANL2DZ	0.9393	49	
MP2/6-31G(d)	0.9434	63	4
MP2/6-31G(d,p)	0.9646		
MP2/pVTZ	0.9649	70	
QCISD/6-31G(d)	0.9537	37	2
BLYP/6-31G(d)	0.9945	45	2
BLYP/6-311G(d)	1.0160	38	
BLYP/LANL2DZS	1.0371	47	2
BP86/6-31G(d)	0.9914	41	1
B3LYP/6-31G(d)	0.9614	34	
	0.9664	46	
	0.9800		
B3LYP/6-311G(d)	0.9739	38	
B3LYP/pVTZ	0.9726	42	
B3LYP/6-311+G(3df,2p)	0.9890		
B3LYP/6-311++G(3df,3pd)	0.9542	31	
B3LYP/LANL2DZS	0.9978	45	
B3PW91/6-31G(d)	0.9573	34	2
B3PW91/pVTZ	0.9674	43	
VSXC/6-31G(d)	0.9659	48	
VSXC/6-311++G(3df,3pd)	0.9652	37	

To calculate the IR spectrum Gaussian software (Gaussian 09) represents the bonds between molecules as quantum mechanical harmonic oscillators as both have quantized energy levels. The solution to the Schrodinger's equation for the QM oscillator are products of Hermite polynomials and Gaussian function, and Eq. 7 gives the eigenvalues.

$$E = \left(n + \frac{1}{2}\right) h\omega \tag{7}$$

(n is the vibrational quantum number). Eq. 8 gives the frequency of the harmonic oscillator.

$$\omega = \frac{1}{2\pi}\sqrt{\frac{k}{\mu}} \tag{8}$$

The only unknown is k – a force constant – and it can be calculated from the second derivative of the energy with respect to the Cartesian nuclear coordinates (at equilibrated geometry). In my calculations, on top of the harmonic oscillator approximations, where there are analytical solutions to the energy levels, I used the anharmonic oscillator. In that case, the calculations are done in a numerical way. As a result of these calculations one can determine the harmonic and anharmonic frequencies of vibrational modes along with their overtones, and intensities.

For my calculations, the density functional that I used was M06 (Minnesota, 2006). It is a global hybrid functional with 27% Hartree-Fock exchange. It is a fourth

rung method on the Jacob's ladder. The reason for choosing this functional is that it yields the results that are close to the experimental results. The basis set I used was def2-TZVP (It is a triple-zeta valence polarization). It is a recommended set for DFT calculation with light elements.

Matrix Isolation and FTIR

Along with the computational method, an experimental spectroscopic technique was used to characterize the gas phase species. The most powerful method of observing the vibrational and rotational modes of molecules is the mid-infrared (IR) spectroscopy. The applications of the method include identification of unknown molecules as well as their qualitative and quantitative analysis. Infrared spectroscopy is based on the study of how the emitted radiation interacts with the molecular vibrations. As a result of absorption of the photons, a resonance condition allows measuring transitions between the molecular vibrational energy levels. As every molecule has a set of unique vibrational levels, IR spectrum yields a unique combination of features that allows the identification of the molecule (Larkin, 2011).

The output of an infrared spectrometer plots an absorbance or transmission vs. wavenumbers. The absorbance is a result of a frequency resonance that takes place when the vibrational frequency of the molecule matches the absorbed light frequency. For a nonlinear molecule with N atoms, there are 3N-6 vibrational modes, while for a linear species, 3N-5 modes. Additionally, for a frequency mode to be IR active, the dipole moment must change during the vibration. If you consider the CO_2 molecules as an example, it has 4 vibrational modes (3*3-5), however its symmetric stretch is not IR

active because its equilibrium dipole moment is 0. Therefore, the CO_2 molecule has three observable IR active modes. The analysis of the IR spectrum can get more complex than that. In CO_2's IR spectrum, shown in Figure 9, one can see two significant peaks (670 and 2300 cm^{-1}) and smaller peaks between 3600 and 3800cm^{-1}. Upon analysis, there are actually two peaks at wavenumber 670 cm^{-1} (degenerate bending modes), one at 2300 cm^{-1} (antisymmetric stretching) and the small peaks correspond to combination bands of the previous vibrations (features dependent on the 3 vibrational modes).

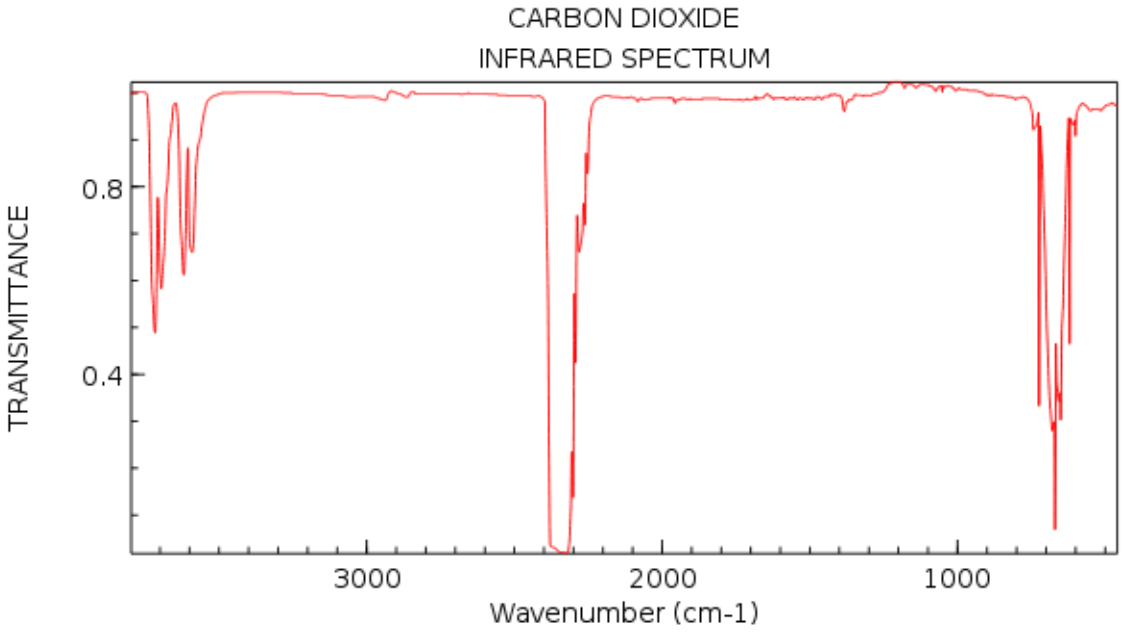

Figure 9. Infrared absorption spectrum of gaseous carbon dioxide (nist.webbook.nist.gov).

It is also possible that overtone bands are observed – absorptions of light that appear at integer multiples of the fundamental frequency bands. However, the intensities of those peaks are weak compared to the normal modes, hence, they are difficult to observe

experimentally.

The frequency of the vibrational modes of the molecules is dependent on the structure of the molecule: masses of particular atoms and the type/strength of bonds between them. A traditional dispersive IR spectrometer uses a monochromator to measure the amount of light absorbed by the sample of interest. In that case, the measurement has to be repeated for every wavelength to produce an IR spectrum. In my experiment, I used a Fourier Transform Infrared Spectrometer (FTIR) and its main advantage is that it uses a Michelson interferometer to collect a full spectrum at all frequencies simultaneously. Additionally, the FTIR has a better signal to noise ratio, shorter scan time, and better wavelength accuracy (Smith, 2011). Figure 10 shows the light path of an FTIR setup using a Michelson interferometer. The light coming from the sources is directed two ways using a beamsplitter: towards a movable mirror (controlled by the computer) and towards a fixed mirror. The two beams are then recombined with a path difference (phase difference) created by changing the position of the adjustable mirror. After the beam is focused on the sample, it is directed towards the detector.

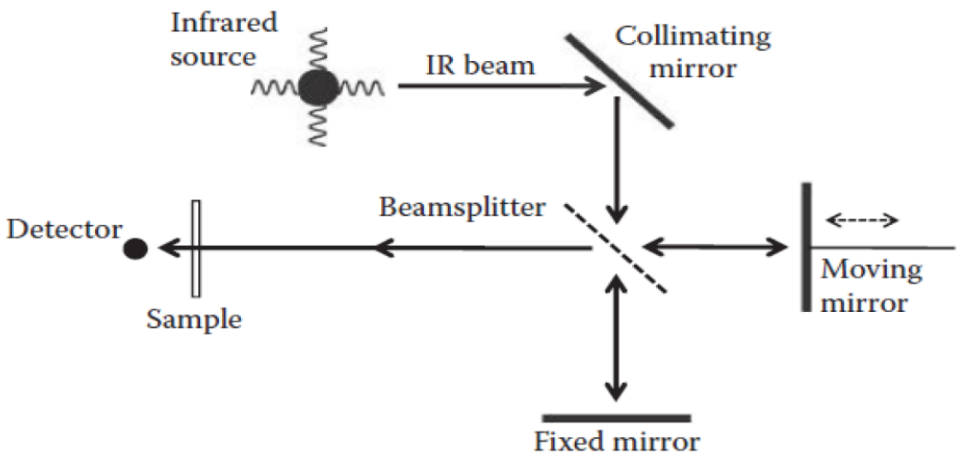

Figure 10. The light path of an FTIR (Smith 2011).

The signal on the detector is called an interferogram and it shows the light intensity of the beam as a function of the phase difference (movable mirror position). It can be maximized by varying the position of the moving mirror to create constructive and destructive interference of the two beams. Figure 11 shows a sample interferogram and its Fourier Transform (FT). The FT algorithm is represented by equation 9 and it transforms the information from the position space (the light intensity for each mirror position) to a frequency space (plot showing the light intensity for each light frequency).

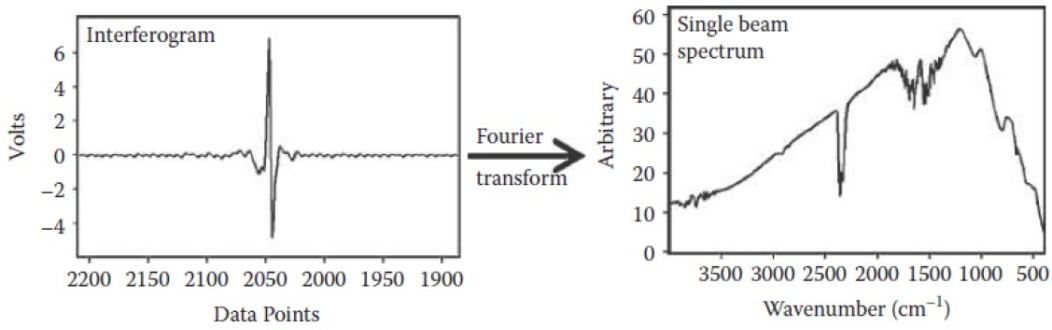

Figure 11. A sample interferogram and its Fourier Transform (Smith 2011).

$$I(t) = \frac{1}{\sqrt{2\pi}}\int_{-\infty}^{\infty} G(k)e^{ikt}dk\,;\; G(k) = \frac{1}{\sqrt{2\pi}}\int_{-\infty}^{\infty} I(t)e^{-ikt}dt \qquad (9)$$

I(t) is a function in position space, and G(k) is a function in the frequency space, which is often expressed in wavenumbers. Following the FT, the resolution of the frequency data is limited by the resolution of the interferogram data, thus the separation in the frequency (wavenumber) space is the inverse of the maximum path difference. As an example, if the maximum path difference is 4 cm, the data in the wavenumber space is separated by 0.25

cm^{-1}. Once the full IR spectrum is achieved, one can start analyzing the particular absorption features, with the light absorption represented by equation 10.

Here the $I_0(\lambda)$ and $I(\lambda)$ are the initial and measured light intensities, N represents the column density of the absorbing molecule (cm^{-2}), and $\alpha(\lambda)$ is the absorption cross section at a particular wavenumber (cm^2).

$$I(\lambda) = I_0(\lambda) * e^{-N*\alpha(\lambda)} \tag{10}$$

$$N = \int_{\lambda_i}^{\lambda_f} \frac{\alpha(\lambda) d(\lambda)}{A_i} \tag{11}$$

The column density can be calculated using equation 11, where I integrate the particular feature from λ_i to λ_f, and divide by A_i, which is a constant known as absolute absorption intensity of band strength and it is a property of the molecule (typically expressed in cm $molecule^{-1}$). By calculating the column density and taking under consideration the area on which I am evaporating the species and the time of the growth, I can calculate the molecular flux on the target, which will be discussed in more details in the results section.

In order to acquire a stable gas sample ready for the IR analysis one needs to "freeze" the gas in an unreactive host matrix – in my experiment, an argon matrix cooled down to the temperature of 10-20 K. The method is called matrix isolation and it allows an in-depth analysis of the molecular structure of the species. G. Pimentel and G. Porter (Pimentel, 1954) first used the matrix isolation technique. It is based on mixing the sample of interest with an excess of an unreactive gas with a suggested ratio of host/guest

of at least 1000:1 (Pimentel, 1954). It is performed on a surface of a material that is cooled down to a temperature that would prevent any diffusion. That way the sample molecules are "stuck" in their positions while being separated from each other by argon gas. That has a purpose of preventing any further chemical reactions. The technique is based on the premise that the host matrix is unreactive; therefore, noble gases such as argon or neon are commonly used. Additionally, the noble gases are completely transparent in the IR range, which allows an in-depth analysis using a FTIR. Even though matrix isolation is the most common experimental method to analyze gas phase molecules, it has some limitations.

Firstly, to be able to use the matrix isolation for nonvolatile substances like metals, a special way of controlled evaporation is required (appropriate ratio of gas/host is a key factor). The presented work used the Knudsen effusion method, which is going to be discussed further in this section.

Secondly, when analyzing the gas molecules in a matrix with a FTIR, the molecule is not in its natural environment. The gas is created in an isothermal cell, but it is analyzed in an "artificial" environment of argon matrix. The transfer of the molecules may in some way impart the properties of the gas, therefore when drawing conclusion about the gas natural environment, extreme caution is required. Additionally, it has been shown that the matrix interacts with the trapped species and might change the vibrational spectrum of the molecules. Red and blue shifts have been proven to appear, with the red shifts being more common (shifts to lower frequency).

The crystal lattice of the inert matrices is arranged in the close packed structure in order to maximize the van der Waals interactions between them. As trapped molecules

can take different locations in the inert matrix, the closest neighbors to the trapped species might be at different distances, which would cause perturbations in the molecules energy levels. For a perfect crystalline Argon at 4 K, there are three possible sites where the molecules could be trapped. The substitutional hole (taking a spot of one of the Argon atoms) with a diameter of 3.75 angstroms, octahedral and tetrahedral holes with diameters of 1.56 and 0.85 accordingly (Batchhelder 1967; Peterson, 1966; Losee 1968; Sears 1962; Greer 1969). However, as the argon matrix is formed by rapidly cooling the gas to 10-20 K, it does not have enough time to form a perfect crystalline structure which causes additional dislocations. That can lead to changing the potential of the matrix therefore affecting the vibration frequencies and making the spectrum more complex.

When the ratio of argon to the species is less than 1000:1, aggregates can be formed in the ice (Hallam 1973). If interaction between the species occurs, a shift of the peaks can be expected. Different types of interaction could give rise to multiplets, making the spectrum more complex. In case of diffusion, molecules of interest would migrate towards each other forming dimers and possibly trimers. As the diffusion progresses, the features representing the dimer and trimers will increase at a cost of the monomer peaks decreasing (Hallam 1973).

All of these effects could lead to shifts, broadening and weakening of the spectral features. Despite these limitations, matrix isolation is the preferred experimental method to set up the molecular analysis of an unstable gas species.

Knudsen Effusion Cell

As mentioned earlier, a special method of controlled evaporation must be used

for metals: the Knudsen Cell Effusion method. It is a technique commonly used to determine the small vapor pressures and characterize the thermodynamic properties of equilibrated vapor and condensed species. It was first published by Knudsen et al. and it was based on the kinetic theory of dilute gases (Kennard, 1938), which allows calculating the molecular effusion flux of vapor species Z_e, that flows from an orifice (area A_0) of an isothermal cell with equilibrated condensed and gas phases inside. The Isothermal cell with a thin edged orifice is a Knudsen effusion cell. A fundamental representation of the effusion flux density in the units of molecules per second per unit area is given by Equation 12, which includes an average thermal speed of a molecule of mass m, in the equilibrium gas with a uniform molecular density ν.

$$Z_e = \nu \sqrt{\frac{kT}{2\pi m}} \tag{12}$$

An equivalent and more practical equation 13 represents the molecular flux out of an ideal Knudsen effusion cell in terms of the temperature T, the mass rate effusion dw/dt, an orifice area A_0, and the vapor pressure of the condensed phase P; k represents the Boltzmann's constant.

$$P = \frac{1}{A_0} \frac{dw}{dt} \sqrt{\frac{2\pi kT}{m}} \tag{13}$$

The formulas 12 and 13 were proven by Knudsen to be suitable expressions to represent

the effusion of vapor in the range of my interest: the micron and lower pressure regions (Knudsen 1950). The formulas hold for the low vapor pressures inside of the cell because the gas molecules that go through the orifice can move independently of each other (long mean free path), therefore not affecting the equilibrium conditions inside of the cell. When the vapor pressures are of higher magnitude, the gas molecules behave like a fluid and distort the equilibrium inside of the cell (Carlson 1967). To reach an equilibrium in a Knudsen effusion cell, three important conditions must be satisfied. Firstly, to make it a time-independent process, the evaporation of the sample needs to be continuous and at a rate much higher than the effusion rate out of the cell. Secondly, as the vapor pressure is a function of temperature, it is important to maintain a stable and uniformly distributed temperature. Lastly, even though it is very difficult at temperatures above 1700 ˚C, the cell itself cannot interact with the sample inside, as it would interfere with the results. The Whitman-Motzfeldt equation (eq. 14) summarizes the factors, which make the Knudsen cell design successful. It is desirable for the ratio of P_e/P_m (equilibrium to measured vapor pressure) to be as close to unity as possible. It is achieved by manipulating the relative dimensions of the orifice and the wall containing the orifice, C/D, and the Clausing factors for the cell and the orifice: W_C and W_D (coefficients representing the fraction of molecules escaping the orifice or the evaporating cell normalized to the incident flux) (Whitman 2012; Motzfeld 2012).

$$\frac{P_e}{P_m} = \frac{W_C C}{D}\left(\frac{1}{\alpha_V} + \frac{1}{W_D} - 2\right) \tag{14}$$

Where α is the vaporization coefficient of the material. As none of these conditions are

trivial, the measures taken to achieve them will be presented in the experimental section of the thesis.

For a gas in equilibrium all directions of motion are equally probable, therefore the motion of the molecules is represented by the cosine distribution. The distribution of modified by a geometrical factor dependent on the relative dimensions of the cell and the orifice. Figure 12 shows how the molecular distribution changes depending on the shape of the orifice.

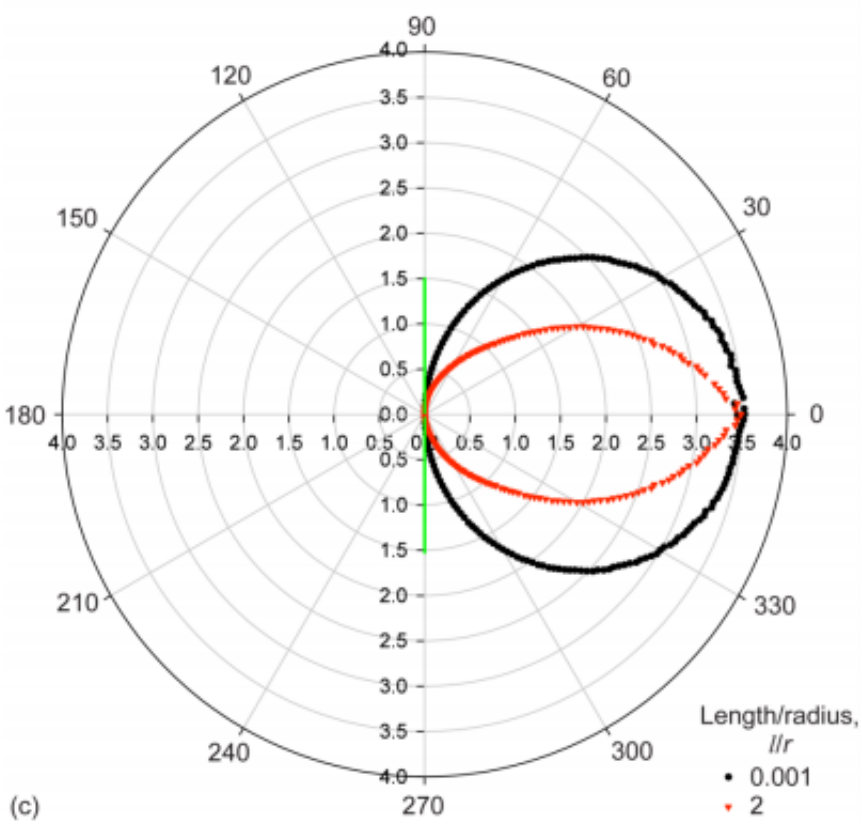

Figure 12. Cosine distribution modeled by a Monte Carlo simulation for a thin (black) and a channel (red) orifice (Copland and Jacobson, 2010).

The Knudsen effusion cell is a crucible made from Tantalum. This refractory

metal is a common choice for a Knudsen effusion cell for several reasons. Tantalum's melting point of 3020 C at atmospheric pressure, allows heating the crucible up to temperatures of 1500-2000C without a concern about melting the crucible. Tantalum is a hard metal but also reasonably easy to machine. It is used in high temperature applications, along with tungsten and iridium, as it is impervious to chemical attack. The detailed schematic of the Knudsen cell will be shown in the laboratory section.

For additional analysis of the vapor in the chamber, I used a mass spectrometer. The principles of operation of a mass spectrometer can be divided into a few stages. First, the vapor species in the chamber are ionized into positive ions. It is done by bombarding the vapor species with electrons emitted from a metal wire with low work function (thoriated tungsten filament) and attracted by a grid, which is positively charged with respect to the filament. Then the positive vapor ions are repelled by the positively charged grid, attracted by a focus plate, accelerated to the same kinetic energy and focused to a single ion beam using the DC and RF voltages (called ion filter). Lastly, the species are directed into a magnetic field that deflects the trajectories of the ions depending on their masses. The lighter the ion is, the more it is deflected. The deflection also depends on the charge of the ions (it could happen, that the electron bombardment in the ionizer will produce a positive ion with the charge greater than +1). Having said that, it is the mass/charge ratio that determines the deflection of the ion and allows the identification of the species. When the positive ion hits the detector it causes the emission current which is later amplified and interpreted by the software as a specific mass/charge ratio. The resolution of the available instruments is determined by the ion filter energy and the standard resolution is the 0.5 atomic mass units where the unit is 1/12 of the mass

of a carbon-12 atom.

All of the concepts described above lay the theoretical ground for the experimental part of the research, which is discussed in detail in the following section.

EXPERIMENTAL

In this section, the experimental details of the laboratory setup will be discussed. The system is built around a spherical chamber custom made by Kurt J. Lesker Company. I used a stainless steel chamber that was to electropolished to minimize the contamination and reach the highest vacuum possible. The design of the chamber is shown in Figure 13.

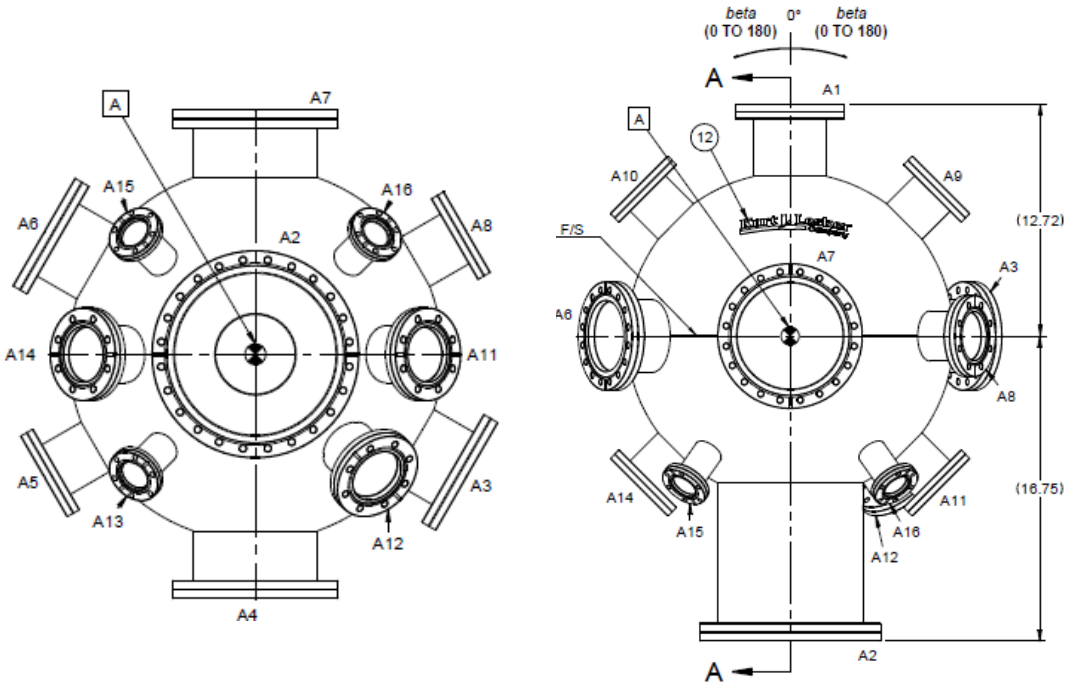

Figure 13. The bottom and side view of a spherical chamber made for the purpose of the experiment.

In the next few paragraphs I am going describe in detail the following elements of the setup and their significant scientific parameters: the e-beam evaporator, the IR thermometer, the FTIR with its optics system, the mass spectrometer, the ion pressure gauge, the cryostat, the argon gas manifold.

E-beam Evaporator

The two most common methods of evaporation are resistive heating and using an electron beam evaporator. The first method is relatively simple: a large amount of electrical current is passed through a resistor that heats up until a desired temperature is reached. The disadvantage of this method is the lack of uniform heat distribution, which creates a temperature gradient in a sample. Further limitations of resistive heating are derived from an expression that describes the heating power: $P = I^2R$. To produce large power, a great amount of current needs to be passed. A high current of the order of 50 amps and above requires extreme safety precaution as well as special wires and feedthroughs that can withstand it. Therefore, the heating elements grow bigger, and without a way to direct the emitted heat, the amount of heat dumped into the system increases. The resistive heating method is much less efficient than e-beam; therefore, the latter one was used.

The principle behind electron beam heating is that free electrons, which are manipulated by electric and magnetic fields, convert their kinetic energy into heat upon colliding with the solid-state material. The electrons travel in the vacuum from a stable thermionic electron emission source (hot cathode) to the evaporation material (anode). To direct the electron beam towards the anode, electric and magnetic fields are used. When the electrons reach the anode, heat is created; it is a direct, much more efficient than resistive, method of heating. The e-beam evaporators can reach temperatures up to 2500 C (Akishin 1967).

The hot cathode is typically a fine metal wire. The choice of the material is dictated by its ability to produce a desired stable emission current. Therefore, materials

with low work function – thermodynamic work required to remove an electron from the cathode – are preferred. Passing a moderate amount of current through the filament (cathode) allows the electrons to undergo a thermionic emission, and under an influence of an electric field, they flow towards the anode. The best filaments are made out of refractory metals such as molybdenum, or tungsten, as besides having a low work function, they have a high melting point and a low vapor pressure. To further decrease the work function, a thin layer of substance with an even lower value of work function is coated on the filament e.g. thorium, lanthanum or barium oxide. Additionally, the reactivity of the cathode needs to be considered. The thoriated tungsten filament used in the setup has a work function of only 2.6 eV (Berman, 2014), but should not be used under pressures above 10^{-5} Torr, as it is very susceptible to oxidation.

As the anode plays a key role in a successful evaporation process, it is important to pick a material with the properties fitting its task. Above all, the material must be a great electrical conductor, as it needs to be able to supply a bias voltage of 1-2 kV and pass the emission current to the ground. Additionally, to prevent melting which brings about contamination issues, the anode material must be able to withstand high temperature and have low vapor pressure. To lower the temperature of the anode, a cooling shroud with circulating cold water is mounted around the unit. Taking into account all requirements, the refractory metals such as molybdenum or tantalum are ideal materials for the anodes.

The formula $P = V_A I_E$ gives the heating power of the electron beam evaporator, where I_E is the electron emission current (from the cathode) and V_A is the bias voltage of the anode. To control the heating, both emission current and bias voltage can be precisely

adjusted using their own power supplies. To increase the power output, it is preferable to increase the bias voltage rather than the emission current. A high current generates excess heat that could lead to contamination issues as well as a decrease in a lifetime of the emission source. The details with the design and characterization of the e-beam evaporator can be found in a thesis work written by Yarden D. Bosh (Bosh 2015).

The tantalum crucibles used for the experiments were made by Brian Grindstaff, the Missouri State University Machinist. The design of the crucible is based on previous work done by Jacobson on Knudsen Cell effusion and has been revised multiple times in order to optimize the flux out of the crucible. The figures below represent the design used in the experiments.

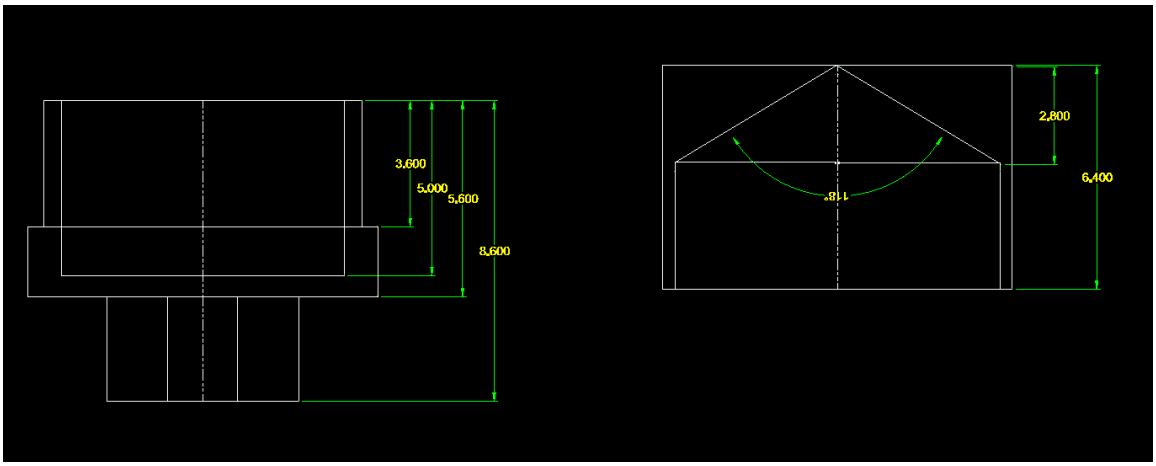

Figure 14. The crucible design in CAD with its dimensions in mm.

The crucibles made out of tantalum, despite having higher melting points than other refractory metals, were a source of contamination in the form of tantalum oxides. As the crucibles were made out of a tantalum rod of the diameter of the crucible, the tantalum oxides formed over a long time on the outside surface of the cells as well as carbon monoxide and dioxide contamination from air. I attempted chemical etching of the

crucibles by using the hydrochloric and nitric acids (1:1 ratio), but the method did not prove effective. An alternative method of heating up the crucible to a high enough temperature to evaporate the oxides, but do not melt the sample.

Based on the phase diagrams of the exoplanet's constituents, the crucibles need to reach temperatures between 1300 and 2000 C. As vapor pressure is temperature dependent, it is essential to have a precise temperature measurement. There are a few challenges associated with the temperature measurement of a Knudsen cell. A thermocouple that is commonly used for temperature measurements, would act as a heat sink upon contact with the crucible. Additionally, physical contact that is necessary for a thermocouple combined with high temperature of the crucible would be a source of great contamination, so I decided against it. A solution to these issues is pyrometry, which does not involve chemical or physical interaction with the cell. An infrared thermometer determines the temperature of a surface from its thermal radiation spectrum; therefore, all I need is a clear line of sight and special windows that do not block any infrared wavelengths. Infrared thermometers can be calibrated by testing them while melting of well-known materials such as gold or silver (Copland and Jacobson, 2012).

The IR thermometer that I used was an Ircon Ultimax Infrared Thermometer UX 10PH. Its reading precision is limited by the output voltage having a range of 0-1 V and step size of 0.01 V. Based on Planck's thermal radiation equation given by formula 15, I could specify the power (B) to temperature dependence for the specific wavelength (λ) that the UX 10PH models emits.

$$B_\lambda(\lambda, T) = \frac{2hc^2}{\lambda^5} \frac{1}{e^{\frac{hc}{\lambda kT}} - 1} \tag{15}$$

The analog output voltage scales as the radiative power at 0.65 microns $P \propto \varepsilon T^{9.63}$ (ε and T represent the emissivity and temperature) and it can be converted to a temperature reading between 900 ˚C and 3000 ˚C. The accuracy of the temperature measurement is +/- 10 C. When reading the temperature, it is important to consider the emissivity of the material. As the emissivity is a temperature dependent physical property of the material, in order to get correct continuous readings, I had to adjust the output by taking into account the changing emissivity of the material (as suggested by Ircon). The measuring wavelength of the thermometer is 0.65 μm. To obtain the emissivity of tantalum for the whole range of temperatures, a polynomial fit was created to the experimentally observed values (Hoch M., Narasimhamurty H. V. I. 1963)

Fourier Transform Infrared Spectroscopy

As the principles of the operation of the FTIR were described in the theory section, the focus of this section will be on the set parameters and additional elements of the FTIR setup. In the experiment I used the Nicolet 6700 FTIR spectrometer to produce vibrational spectra of the samples. As the sample is in the middle of the chamber, in order to direct the IR beam through it, I needed to use an external emission port for the spectrometer. That means that I had to go through the optical path shown in Figure 15.

For the mid-IR light range, the recommended beamsplitter is made out of KBr and so are the windows in the chamber that the light goes through on the way to the MCT-A detector. It is a Mercury-Cadmium-Telluride, cooled by liquid nitrogen, that can read the 12500 - 400 cm^{-1} range. When the IR beam goes through air, it is exposed to molecules of water, CO, and CO_2 that all have strong absorption features in the IR range. To

minimize that effect, the spectrometer as well as the bagged space between the spectrometer and the chamber need to be purged with dry air or nitrogen gas. To achieve "cleaner" spectra I used the FTIR Purge gas Generator supplied by Parker Balston.

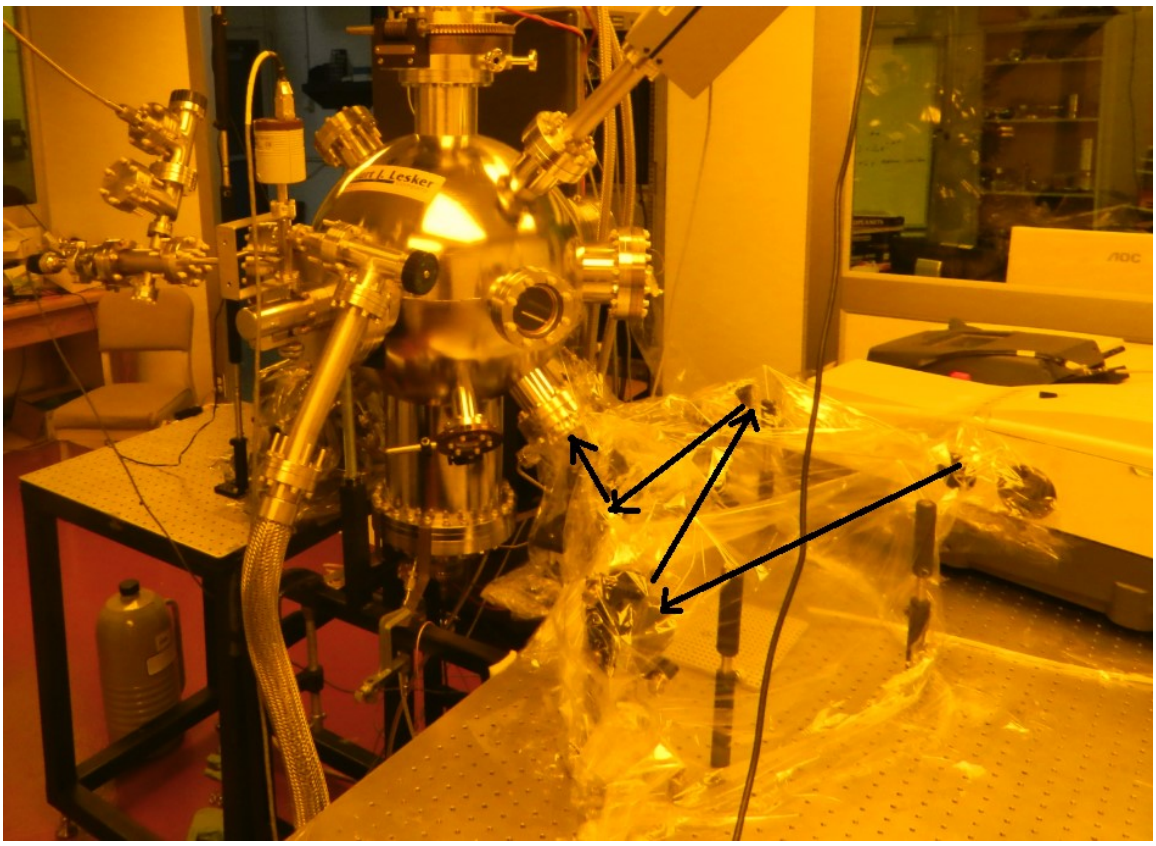

Figure 15. Optical path of the IR beam from the FTIR to the chamber.

When setting up parameters for the spectra, one needs to consider a few factors: wanted precision, data spacing, and signal to noise ratio. The last one can be improved by either increasing the number of scans or setting a higher resolution of one scan (data spacing). To improve the resolution one can change the beam size to smaller, but that will also decrease the signal to noise ratio. I take 128 scans and the final output is the average of all of them. The data spacing is 0.241 cm^{-1} and the aperture size is 9. Another controlled parameter is the optical velocity, which is twice the value of the moving mirror

in the interferometer. The value of 0.693 is recommended for the detector. Increasing the optical velocity will allow you to take the same number of scans faster, but it will also decrease the signal to noise ratio.

Mass Spectrometer

The mass spectrometer used in the experiment is a Stanford Research System RGA series 300 unit allowing tracing the mass to charge ratio in the range of 1 to 300 amu. During the runs, I traced the full available range and recorded all the data. The scans were logged in a pressure vs. time scan with the following settings: the electrons energy in the ionizer is 70 eV, the ion energy, which controls the resolution of the mass filter, is 12 eV and it correlates to 0.3 amu resolution of the scan. In order to optimize the ion sensitivity, the focus voltage is set to its default value of -90 V. To adjust the detectable partial pressures, I followed the guidelines provided by the user's guide, which relates the scan speed parameter of 3 with 0.44 ms per single mass measurement, and $1.5*10^{-14}$A limit. An example of a scan is shown in Figure 16.

As low temperature of the ice matrix prevents diffusion in the ice, it is important to cool the flag to the lowest possible temperature. The system uses an Advanced Research Systems' closed cycle cryogenic refrigerator that is based on the Gifford – McMahon cycle. The DE 202 Expander is connected to the compressor (model HC-4 MK2 by APD Cryogenic Inc.) which supplies the compressed helium and takes out the low-pressure gas. The system, due to extensive use, is capable of cooling down the stage to 15 K.

The gas manifold created in the lab is used for controlled leaking of argon to

create the argon ice. The highly precise leaking valve and a simple 1/8 inch nozzle pointed at the flag is used to grow the argon matrix. The thickness of the ice as well as the rate of growth are monitored by an ice thickness monitor utilizing an interferometer pattern. The pattern is created by a red laser pointed at the flag that goes through the ice and is being reflected of the flag into a silicone diode connected to a current amplifier.

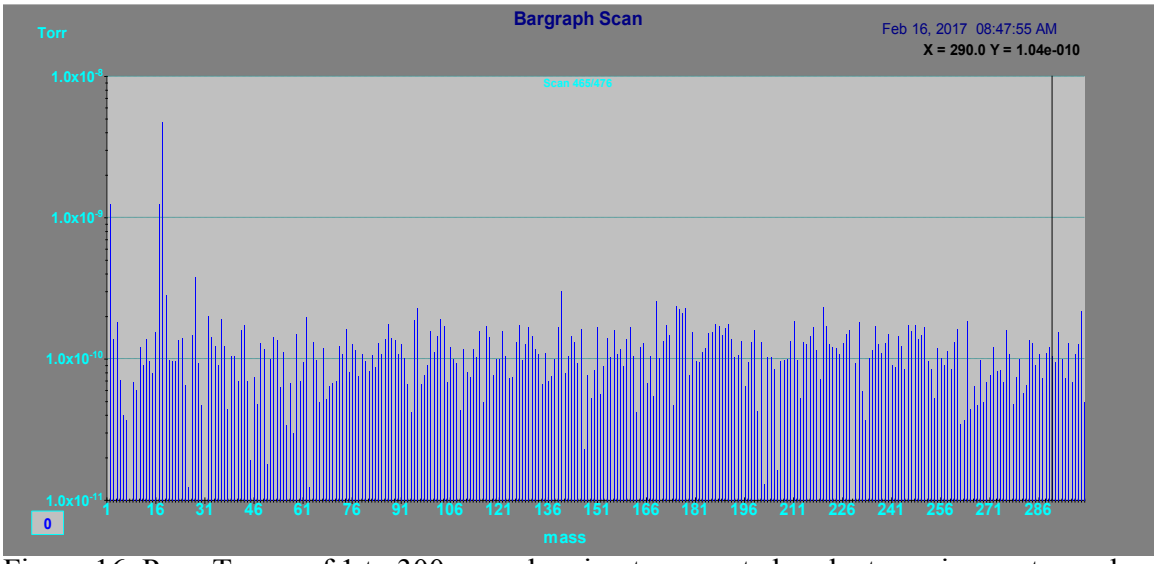

Figure 16. P vs. T scan of 1 to 300 amu showing two most abundant species: water and hydrogen (18 amu and 2 amu accordingly) with corresponding partial pressures of 4.71 $*10^{-9}$ Torr for water and $1.2*10^{-9}$ Torr for hydrogen.

The current is converted into voltage, which will represent constructive and destructive interference of the light beams: one reflected of the surface of the ice and the other one reflected of the flag. One can regulate the ice growth rate by simply leaking in more argon and observing the pattern. The formula that allows the calculation of the thickness of the ice, t is shown by equation 16.

$$t = \frac{k\lambda_{red}}{n_{ice}cos\theta} \tag{16}$$

Where k represents the number of fringes, n_{ice} is the refractive index of the argon ice and θ is the reflection angle (45˚).

RESULTS

This part of the thesis will present the results of the research and will include the analysis of two binary systems: mixture of SiO_2 with Al_2O_3 and SiO_2 with CaO. The aim was to identify the species present in the gas phase above the melts created by extensive heating of the samples. As the infrared wavelength is used for astronomical observations, I hope that my results will aid the interpretation of the data acquired by the telescopes. The absorption data, including the location of the lines as well as the opaqueness or cross–section absorption, is an important input for modeling of hot earths' atmospheres. The results consist of the spectral features identification, the mass spectrometer analysis and the computational simulations for both binary systems. Each experiment was performed twice, and the majority of the features have been identified.

Al_2O_3 and SiO_2

The sample composition was chosen based on the gas phase diagram from the Sixth Edition of Data of Geochemistry: Phase-Equilibrium relations of the Common Rock-Forming Oxides except water. The diagram is shown by figure 17 and the "X" on the figure represents the concentration and temperature I aimed for. Based on the phase diagram, at the 80:20 molar percent ratio of SiO_2:Al_2O_3 and at the temperature above 1780 ˚C, all species should be in the liquid or gaseous phase or a combination of both. According to research done so far, the evaporation of SiO_2 results in SiO and O with the enthalpy of vaporization of 481 kJ/mole (Hidalgo 1960; Bondar 2005). The evaporation of Al_2O_3 results with mostly Al atoms, but also AlO, Al_2O and O_2 (Gerasimov et al.

2012). During the evaporation, multiple competing chemical reactions take place, but

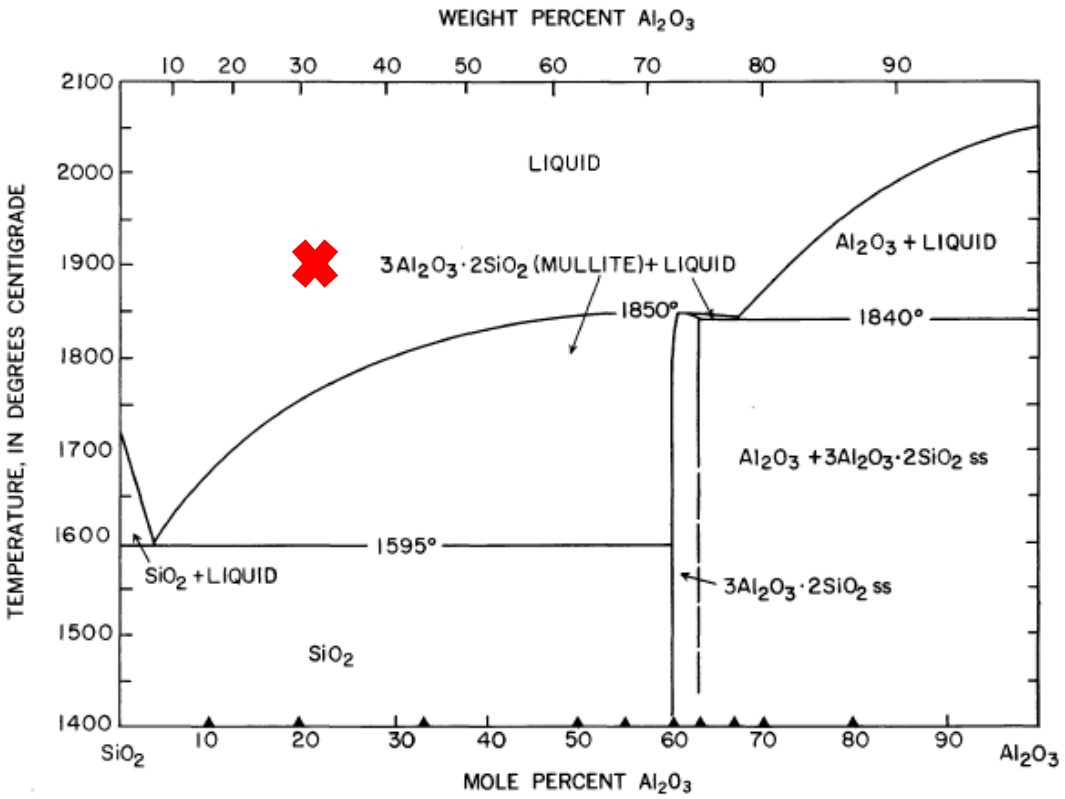

Figure 17. The phase diagram of the binary system of SiO_2 and Al_2O_3 with an X marking the region of interest. The bottom axes represents the molar weight of the constituents.

the most abundant vapor species are SiO and Al. Equation below represents a reaction in the gas phase that takes place between them.

$$Al(g) + SiO(g) \rightarrow AlOSi(g)$$

The change in enthalpy for this reaction at room temperature is -200kJ per mole (Junker, Freisen, Schnockel 2000). The negative sign for the enthalpy change represents an exothermic reaction, which makes it favorable. The data available on this species is

scarce, however my experimental infrared results, mass spectrometer trace as well as computational results confirm the existence of this radical in the gas phase.

In the experiment, the temperature is kept constant and the metal oxides melt as well as the gas phase species are assumed to reach a thermal and chemical equilibrium. Certainly, there are reactions that happen in the gas phase as well as the liquid phase, which can be modeled by codes like MAGMA (theory section).

The gas phase species are sampled using the Knudsen cell effusion method and "trapped" in the argon ice. The starting pressure of the chamber, with the cryostat on, was at $3.0*10^{-10}$ Torr. After the argon gas was leaked at a rate $9.3097*10^{17}$ atoms per second, the pressure increased to $2*10^{-6}$ Torr and the evaporation process was started. In order to estimate the deposition rate from the Knudsen effusion cell, one needs to take into account the contributions from all of the gas species that are in the cell. The sum of the species' vapor pressures is then correlated to the deposition rate on the flag. To simplify the calculations, consider I take the following SiO data: vapor pressure of 1 Pa at 1900 ˚C (Iosilevskiy, 2014), and evaporation at a distance of 0.186 m away from the flag, I get the deposition rate of $2.7774*10^{16}$ molecules per second. The ratio of argon to the evaporated species is estimated to be 33:1 and it is below the expected value, however it still allowed us to detect spectral features. The possible effects of a low ratio of argon to the evaporates will have to be taken into consideration during the data analysis. For this run, the final temperature was 2000 ˚C, and two IR spectra were taken at that temperature. The final spectrum is compared to the clean, cold background spectrum from before the growth. The temperature of the flag is about 15 K. A result of the spectral math is shown in figure 18 representing the gas phase IR features of species trapped in the argon ice.

The broad features between the 1300 and 900 cm-1 is water ice and it appears due to contamination issues, however masses affect the vibrational modes that include the silicon atom. The higher the mass of an atom, the lower is its vibrational frequency; therefore, the peaks representing heavier isotopes are shifted towards lower wavenumber values.

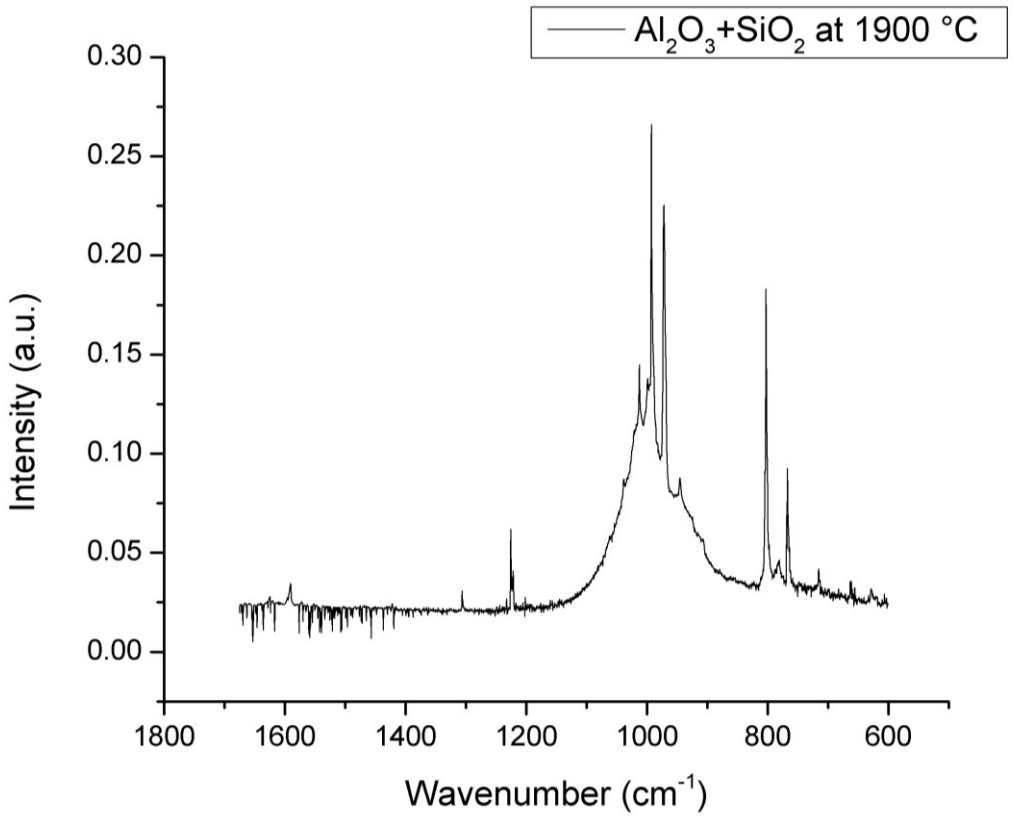

Figure 18. Infrared spectrum in 1800-500cm^{-1} range for the Al_2O_3 +SiO_2 binary system.

Assuming the conditions for the matrix isolation and Knudsen effusion are satisfied, infrared spectrum can be used to calculate the vapor pressure of the species in the Knudsen cell. I will give an example of this calculation further in this section.

To perform an analysis of the IR spectrum, one needs to take under consideration all of the other the peaks as some of them might correspond to the same molecule. To identify a species with confidence, it is key to know how many modes of vibration each molecule has (explained in detail in the theory section). Given the absorption strength per molecule (cross-section per molecule), the area under a peak can be correlated to the column density of the species (molecules per area). Then, knowing the total time of the evaporation, the molecular flux can be calculated, which obeys the cosine distribution out of the crucible's orifice. Knowing the flux at the orifice, it is possible to calculate the vapor pressure of the species.

The analysis starts with identifying the existing gas phase species. Table 4 shows a summary of peak analysis from the Al_2O_3 +SiO_2 binary system.

Table 4. Experimental data from the Al_2O_3 +SiO_2 system at 1900 ˚C.

Species	Position (cm^{-1})	Integrated area (experimental)	Integrated area (Gaussian)
AlOSi	1012.92 ± 0.018	0.10663 ± 0.005	15720
Al_2O	992.94 ± 0.01	0.063647± 0.002	N/A
AlO	945.6 ± 0.01	0.05562± 0.00179	8949
SiO	1225.87 ± 0.01	0.2152± 0.0104	2075
Si2O2	802.9043± 0.04433	0.7204	6427
Si3O3	972.2526	1.318 0.024	66700

The plots of the spectroscopic features characterized in table 4 are shown in figures 19 and 20 side by side the calculated Gaussian spectra.

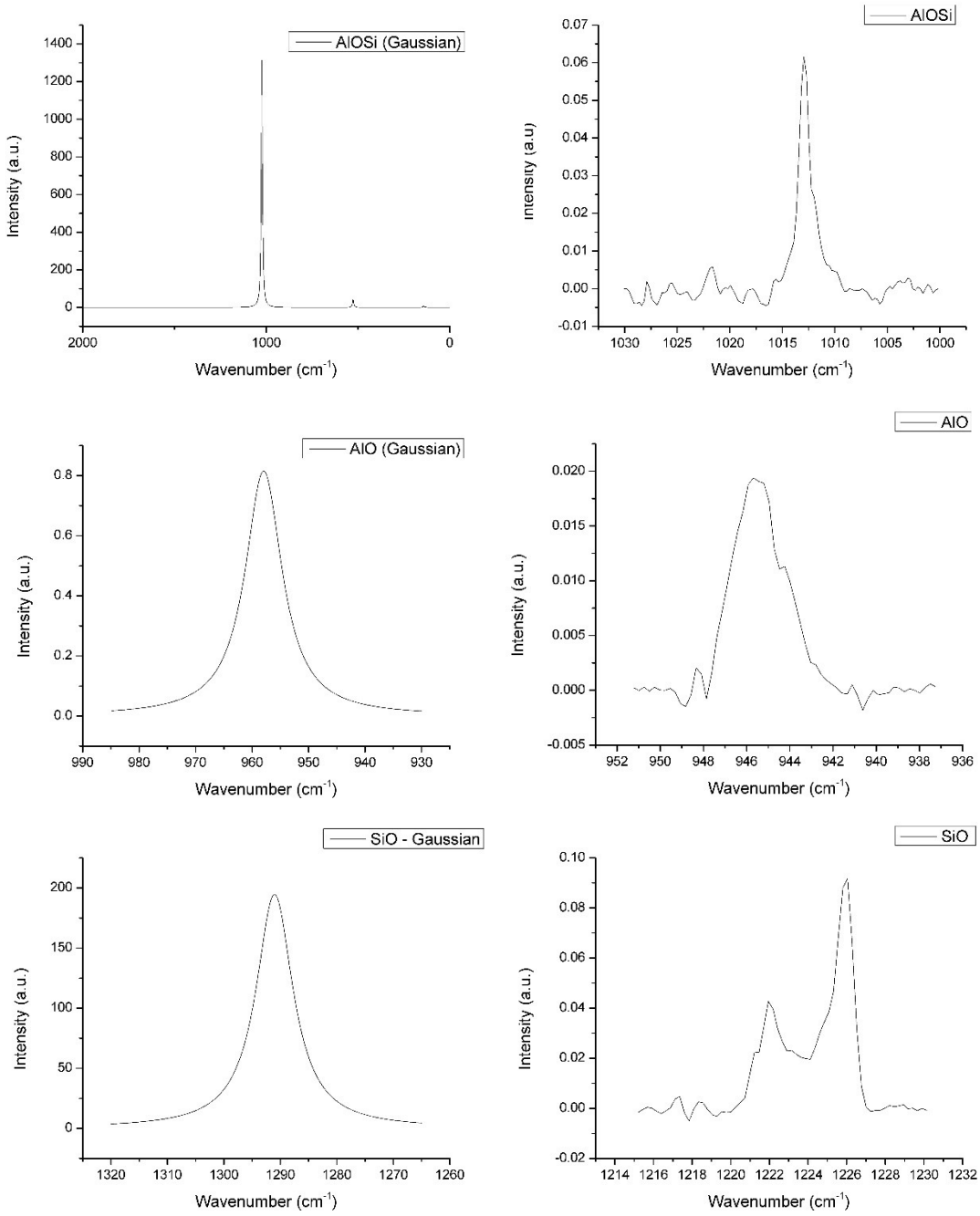

Figure 19. Comparison of the computed spectra (left) with the experimental feature (right) for the following species: AlOSi (top), AlO (middle) and SiO (bottom). Close agreement of the calculated features confirms the identification of the vibrational modes. Data corresponding to these peaks is presented in Table 4.

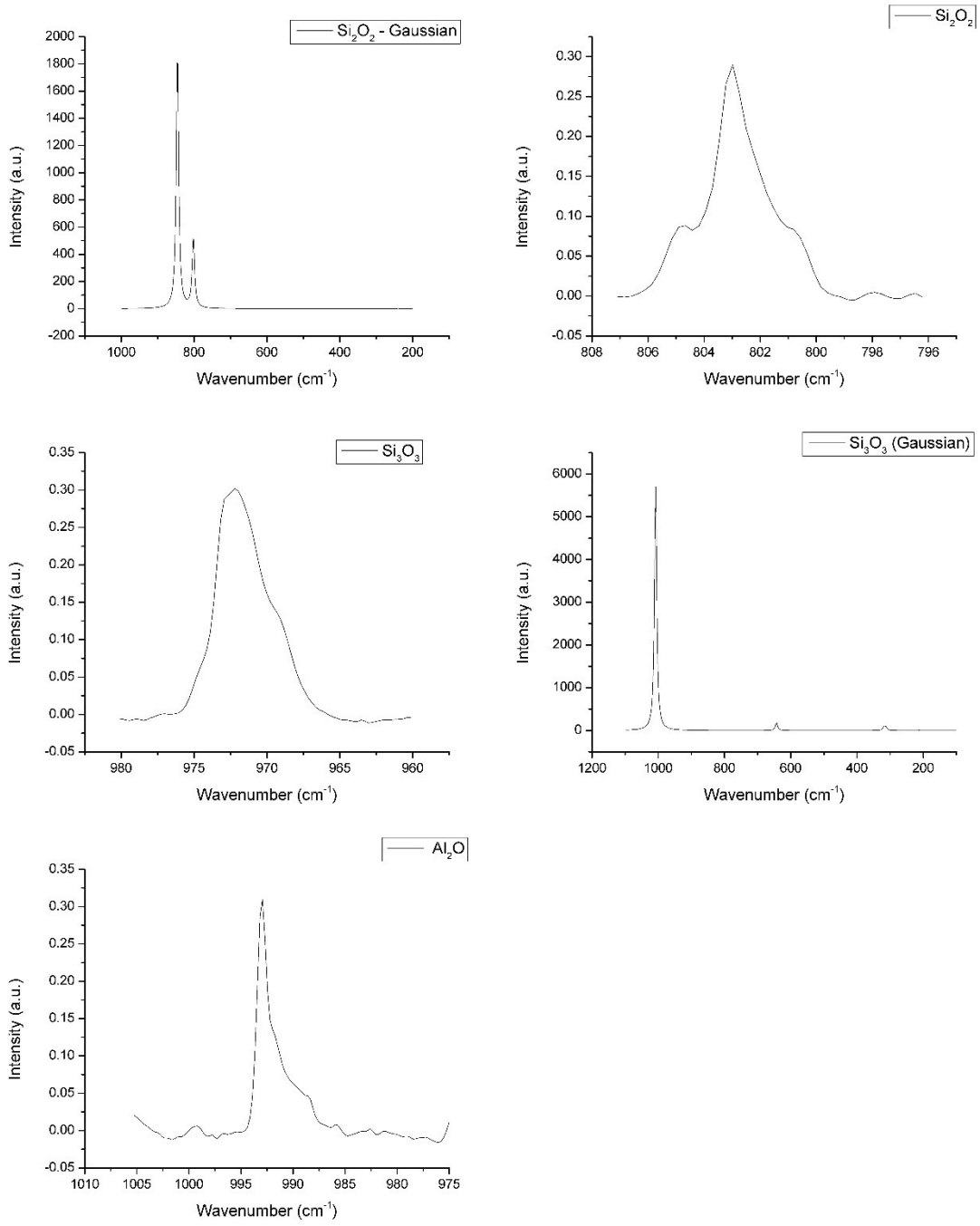

Figure 20. Comparison of the computed spectra (left) with the experimental feature (right) for the following species: Si_2O_2 (top), Si_3O_3 (middle) and Al_2O (bottom). Close agreement of the calculated features confirms the identification of the vibrational modes Data corresponding to these peaks is presented in Table 4.

The computed IR spectra were used to identify some of the vibrational modes. To show the analysis by comparison, a Gaussian-generated spectrum and the experimental figure for the vibrational modes for the particular species are presented side by side in figures 19 and 20.

During the analysis of the IR spectrum, it is important to consider the abundances of the isotopic species of the elements. As an example, 92% of silicon has a mass of 28 atomic mass units (^{28}Si), 4.3% is in a form of ^{29}Si and 3% is ^{30}Si. These three different To be more specific, when considering the frequency of a particular bond of the molecule, a quantum harmonic oscillator with its quantized energy levels is used as its representation. The frequency of the harmonic oscillator is inversely proportional to the square root of the reduced mass of the bonded atoms. If this interpretation is applied, it is possible to estimate the location of the isotopic peaks of a molecule. For example in SiO, the reduced mass with ^{28}Si is 3.1909 amu and with ^{29}Si, it is 3.211 amu. Following the harmonic oscillator approach, if the ^{28}SiO is centered at 1225.8 cm^{-1}, the ^{29}SiO peak should be centered at 1218.1 cm^{-1}. The experimental data is in an acceptable agreement with the harmonic oscillator approximation: ^{28}SiO is centered at 1225.8 cm^{-1} and the ^{29}SiO peak is centered at 1221.95 cm^{-1}. The possible reason for shifts in the matrix ice were discussed in the theory section.

My experimental data does not show all the peaks that the calculated spectra do, and that is for a few reasons: some features are in the range where the noise is far too big to see the features (below 600 cm^{-1}), or the intensity of the vibration is just too low to be detected. The molecular intensity of the IR is dependent of the dipole moment change that is caused by vibrations of the atoms. There is scarce experimental data on the

absorption coefficients of gaseous species such as SiO or AlOSi however, as suggested by the literature review, I was able to perform a semi-quantitative analysis of the abundances of the molecules and the cross-section areas. In the next few paragraphs, the focus will be the AlOSi analysis.

An important aspect of an isotopic analysis is considering that the ratio of the natural abundances of elements should be equivalent to the ratio of areas under the peaks assigned to particular isotopes. For example, after a fitting procedure of the AlOSi feature, the ratio of the areas of $AlO^{28}Si$ and $AlO^{29,30}Si$ is equal to 7.08, which considering the matrix effects, is an acceptable value. Due to the data resolution and possible shifts in the matrix, the ^{29}Si and ^{30}Si combine into one peak at lower frequency than the most abundant, lighter isotope. The fitting result is shown in figure 21 and its details are given in table 5.

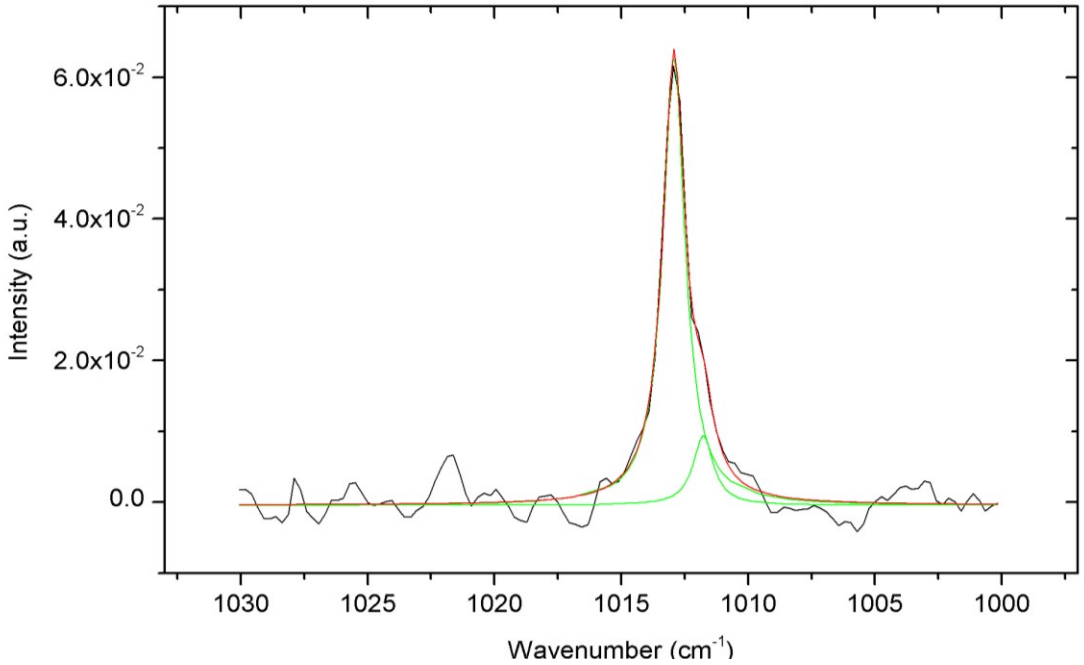

Figure 21. AlOSi feature fitted with two Gaussian functions using the Origin Software peak fitting tool.

Table 5. AlOSi peak fitting data using Origin Software.

Species	Position (cm^{-1})	Natural abundance of Al, O, and Si (%)	Integrated area (experimental)
$^{27}Al^{16}O^{28}Si$	1012.92 ± 0.018	100, 99.7, 92	0.10335 ± 0.005
$^{27}Al^{16}O^{29,30}Si$	1011.76718 ± 0.11	100, 99.7, 7.3	0.01496 ± 0.002

Ab Initio calculations of position and strength have been considered a sufficiently accurate prediction of the vibrational characteristic of a material (Botschwina and Rosmus 1985; Ziegler 1991; Labanowski and Andzelm 1991). For my calculations I used the Gaussian program and the details of the calculations are given in the theory section.

The Gaussian generated plots are shown in figures 20 and 21. The integrated area under the peak is dependent on dipole moment change and can be interpreted as a cross-section area or molecular absorption (cm^{-2} mol^{-1}). By comparing the calculated SiO and AlOSi features' areas (per molecule), one can determine the relative absorption coefficient of an AlOSi molecule with respect to the SiO molecule. After integrating both calculated peaks, the ratio turned out to be 7.8. This analysis combined with the experimental areas' ratio (0.5) results in approximately 1 AlOSi molecule per 16 SiO molecules.

Even though the Al_2O_3 +SiO_2 binary system has been extensively investigated, there is not much data on AlOSi. One of the reasons could be that the initial composition of the sample varies from the one typically used. A lot of the work has been done with mullite as the initial composition: Al_2SiO_5, $AlSi_2O_5$, $Al_3Si_2O_{13}$. The gas phase species above mullite, confirmed by the high temperature mass spectrometer studies are: SiO, Al, AlO, Al_2O, SiO_2, and AlSiO (Shornikov et al., 1994; Shornikov et al., 2000; Shornikov

and Archakov, 2000). Additionally, the vapor pressure analysis over mullite suggests the ratio of 1 molecule of AlSiO per million of SiO (Shornikov 2001, 2013). The linear fits to the vapor pressure data of both species are shown in Figure 22.

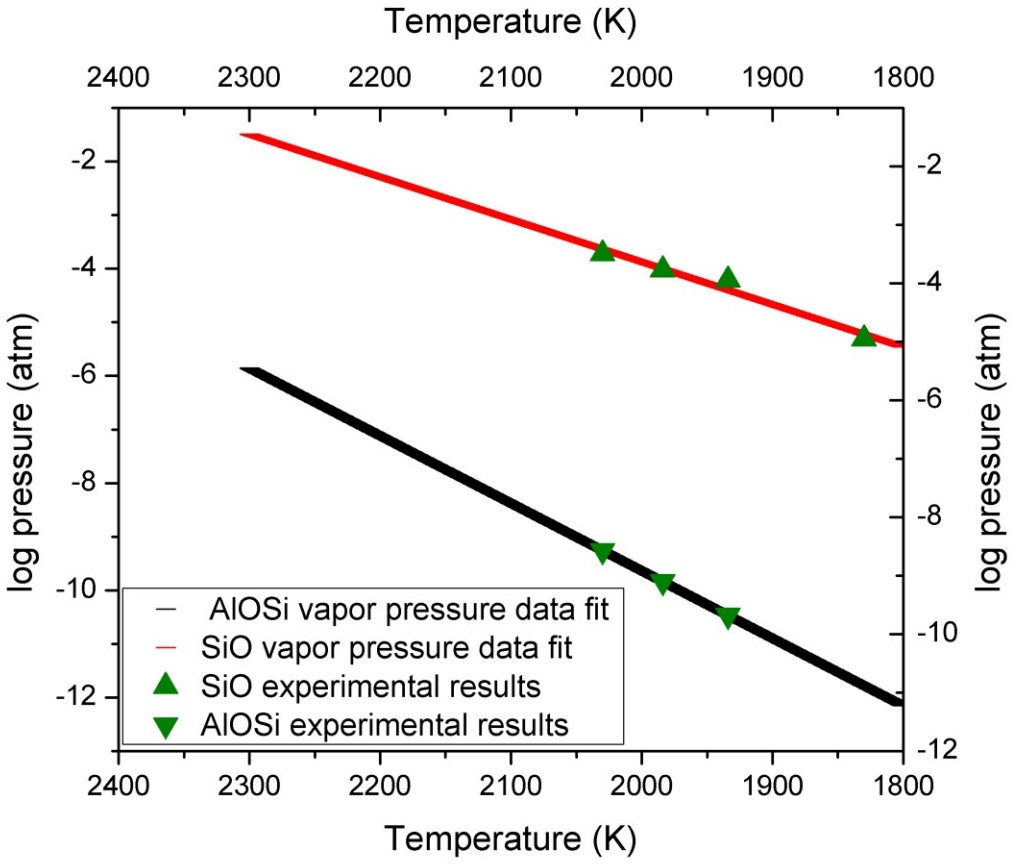

Figure 22. A linear extrapolation of the vapor pressure data indicates that at 2173 K (1900 ˚C), the ratio of SiO to AlOSi is approximately $10^{4.5}$ (Shornikov 2001, 2013).

To sum up the discussion on AlOSi, the results for two different initial compositions of the sample (mullite versus Al_2O_3 with SiO_2) yield very different results. Shornikov's AlSiO/SiO ratio ends up around 10^5, while the AlOSi/SiO ratio from my experiment ends up around 1/16. The conclusion seems to be that the vapor phase species depend closely on the initial composition of the sample.

As mentioned earlier, it is possible to calculate the vapor pressure of the gas phase species from the infrared information. For SiO, given the absorption coefficients found in the literature (Botschwina and Rosmus, 1985) and knowing the growth time of SiO, and the integral of the feature, the molecular deposition rate of SiO on the flag results in.5.7103e+15 molecules per second per cm^2. Then, by applying the cosine distribution, the flux out of the orifice is approximately 6.914e+15. From equation 14, it is possible to determine the vapor pressure for SiO. The calculations based on experimental data resulted in 10 Pa, which is reasonably close to the values found in the literature.

Lastly, the mass spectrometer was used as a tool that helped track the species inside of the chamber. The trace of AlOSi (mass/charge equal to 71) is shown in Figure 23 and it was used as an additional detection evidence of vapor species.

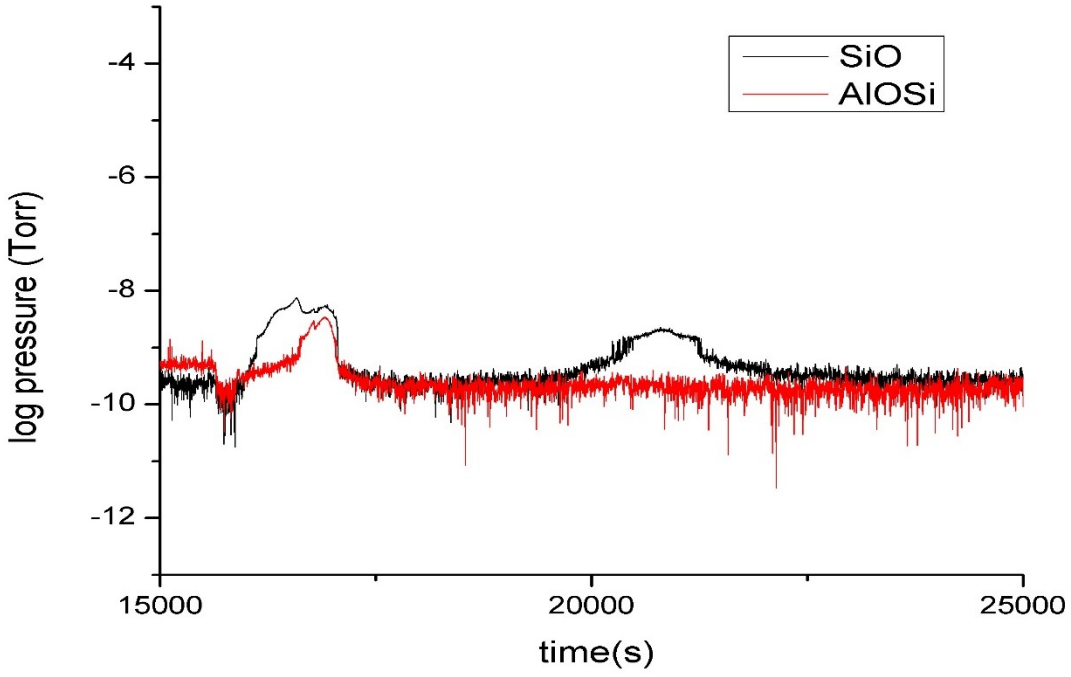

Figure 23. AlOSi and SiO/CO_2 traces on the mass spectrometer pressure vs. time plot.

At this point in research, I only traced specific mass/charge ratio and I was not aware of the AlSiO/AlOSi debacle. If this experiment is to be redone, tracking the mass/charge equal to 55 (AlSi) pressure will answer the question whether both of the species exist in the vapor phase above the Al_2O_3 and SiO_2 binary system.

CaO and SiO_2

The strategy for this binary system is analogous to the one described in the previous section. "X" marks the initial composition of the sample on the phase diagram shown on figure 8. The initial composition my sample was 48% CaO and 52% SiO_2. For this run, the final temperature was 1650 ˚C, and two IR spectra were taken after the growth. The final spectrum is compared to the clean, cold background spectrum from before the growth. The temperature of the flag is about 15 K. A result of the spectral math is shown in Figure 24. Compared to the previous experiment, the features are significantly smaller because the growth time was much shorter. Table 6 shows all the spectral features seen in the spectrum.

Table 6. Experimental data from the CaO +SiO_2 system at 1650 ˚C

Species	Position (cm^{-1})	Integrated area (experimental)	Integrated area (Gaussian)
$CaSiO_3$*	672.08 ± 0.01	0.1839 ± 0.02	8430
$CaSiO_3$*	906.63 ± 0.02	0.0184 ± 0.02	9357
SiO	1226.0 ± 0.01	0.06209 ± 0.02	2075
Si_2O_2+CaO**	802.98 ± 0.01	0.09462 ± 0.02	6427
Si_3O_3	972.2526 ± 0.01	0.2133 ± 0.02	66700

*peaks not confirmed **peaks are on top of each other (figures 28 (a,b) and 29)

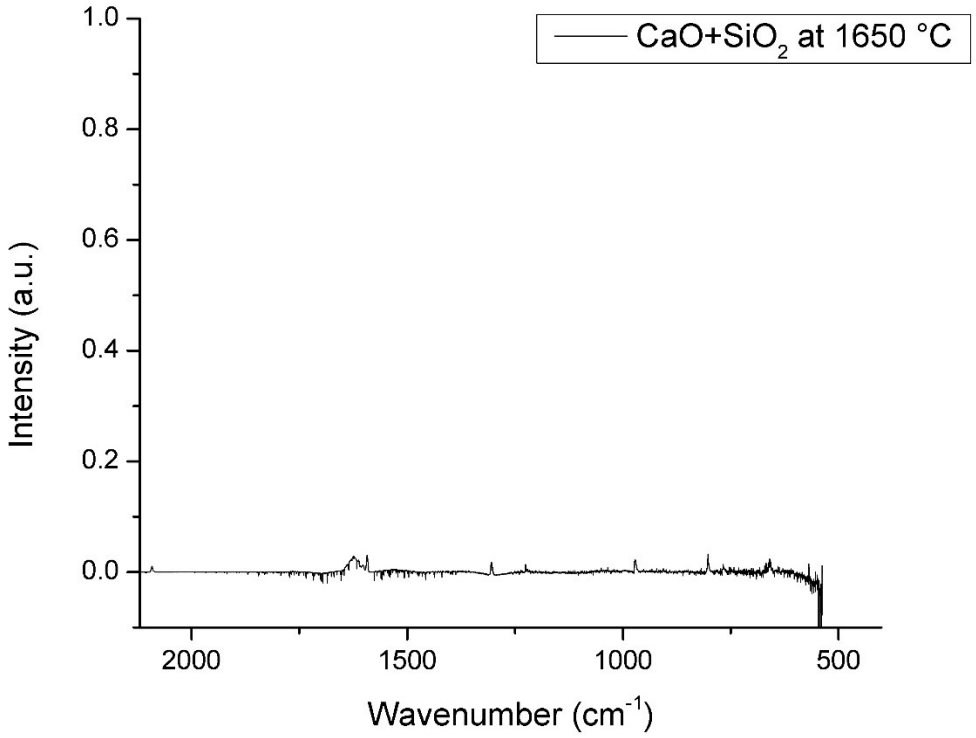

Figure 24. Infrared spectrum in 2100-500cm^{-1} range for the CaO +SiO_2 binary system.

The SiO_2 during its evaporation behaves similarly to the previously discussed system: it dissociates mainly into SiO and O, as well as small amounts of SiO_2. On the other hand, CaO evaporates into CaO, C and O (Lopatin et al. 2008). Figure 25 (a,b) show two features in the experimental IR spectrum that I identify as $CaSiO_3$. This would be the first experimental assignment of the $CaSiO_3$ infrared feature.

The calcium silicate is created in a way represented by a chemical reaction shown below.

$$CaO + SiO_2 \rightarrow CaSiO_3$$

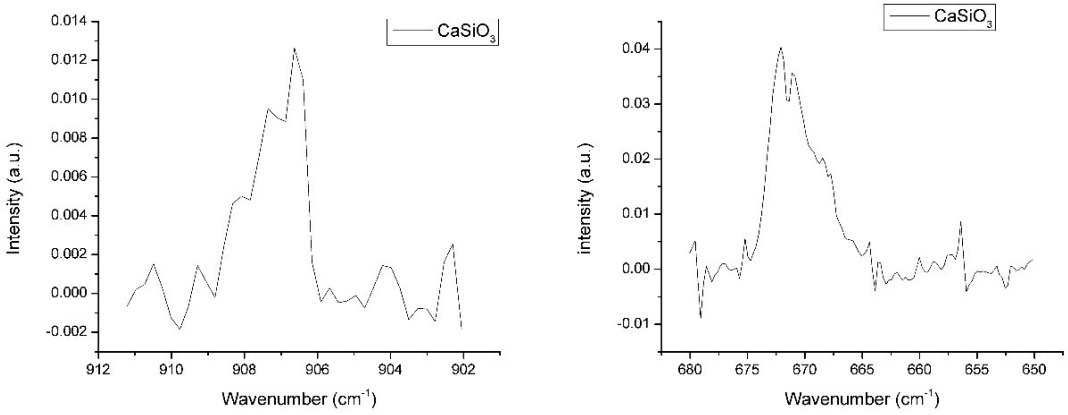

Figure 25(a,b). From left to right: features centered at 906.63 cm^{-1} and 672.1 cm^{-1} that correspond to computed $CaSiO_3$ peaks (figure 26).

The enthalpy of a reaction above was calculated by Lopatin to be – 437 ± 14 kJ/mol. It seems like a very favorable reaction, however, one needs to consider the reactions necessary in order to get the gaseous species of CaO and SiO_2. It turns out that for $CaSiO_3$, the standard enthalpies of formation and atomization are - 715 ± 24 and 872 ± 25 kJ/mol, accordingly (Lopatin 2008). There is no experimental infrared data on the calcium silicate, and it has been identified in the vapor phase only by Shornikov (Shornikov 1993). The comparison between the Gaussian generated spectrum (Figure 26) and the experimental features (Figure 25 a,b) suggest that two small peaks can be assigned to vibrational modes of $CaSiO_3$.

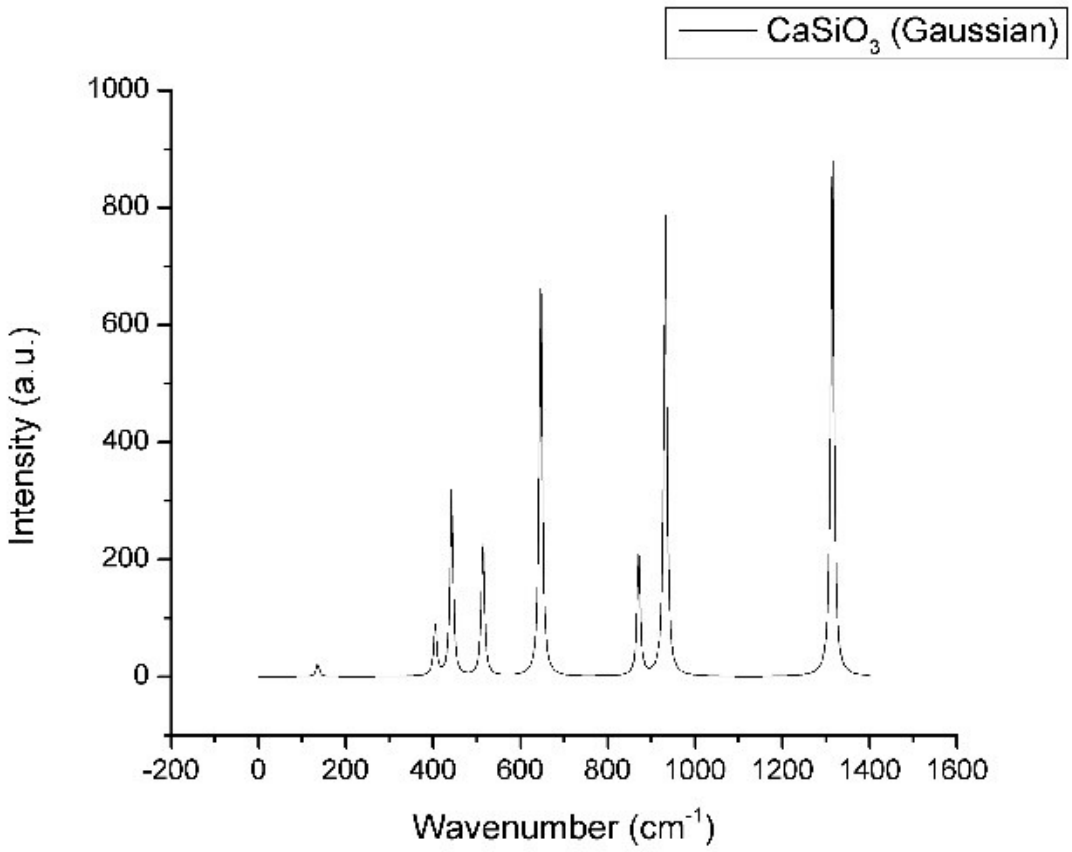

Figure 26. Gaussian generated infrared spectrum of $CaSiO_3$. Harmonic vibrational modes at 932 cm^{-1} and 646 cm^{-1} are close to the experimental values.

Other features that appear in the experimental spectrum were analyzed in the same fashion as in the previous sections experimental spectra are compared to the computed ones. Figure 27 (a,b) represent the calculated peaks of Si_2O_2 and CaO. On the other hand, Figure 28 shows the experimental feature that I think is a combination if Si_2O_2 and CaO. The last feature that was detected in this experiment is the Si_3O_3, which had the same location as in the previous run. Similarly, the same computed spectrum was used to identify it.

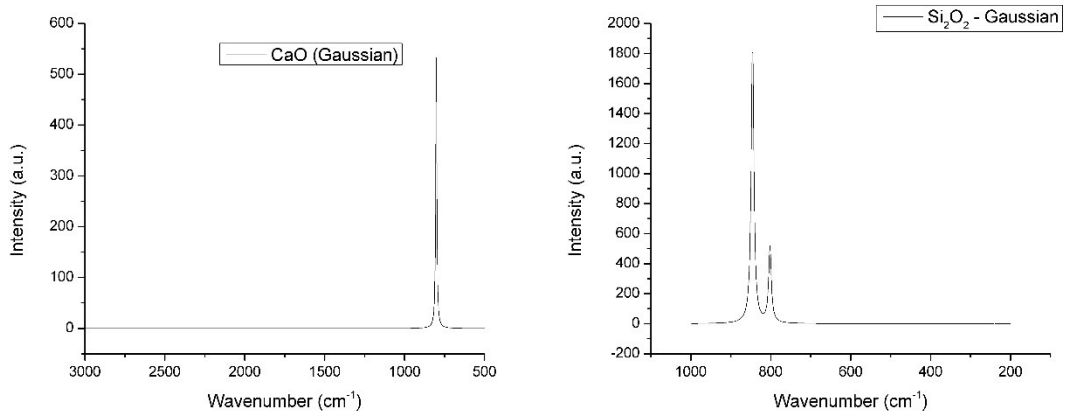

Figure 27 (a,b). From left to right: Si2O2 centered at 845.61 and 801.88 cm-1. CaO centered at 802 cm^{-1}.

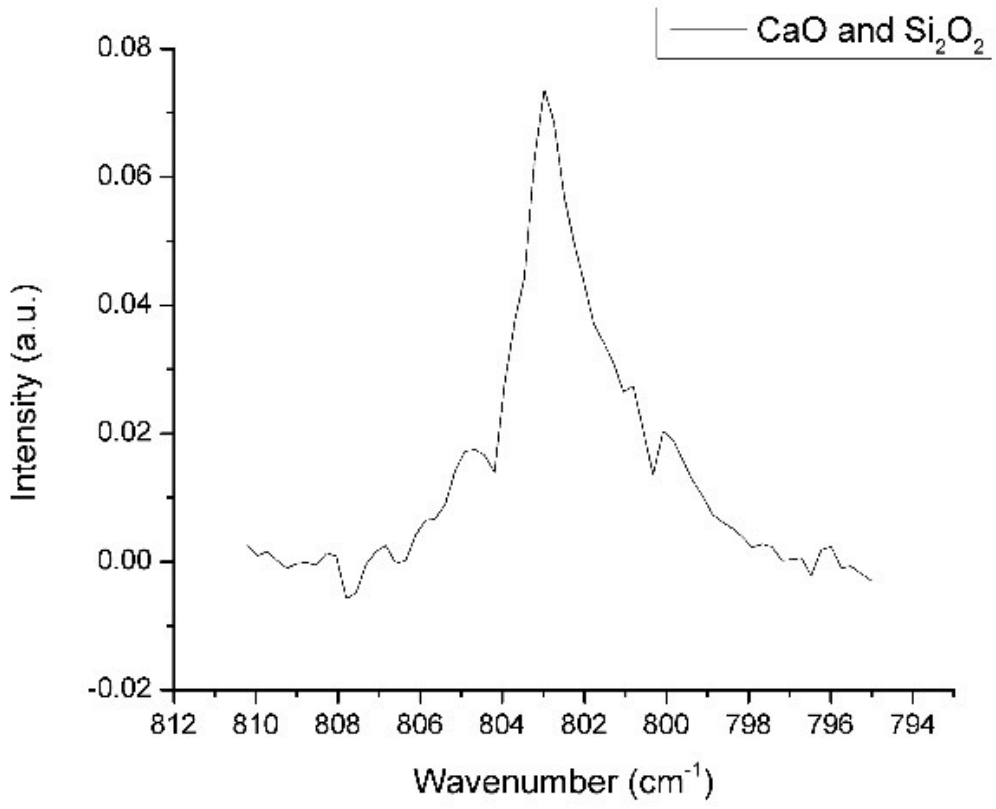

Figure 28. Experimental feature interpreted as a combination of CaO and Si_2O_2.

During this experiment, I ran the mass spectrometer in a mode that records the partial pressure of every mass/charge ratio in the range of 1-300. In order to confirm the $CaSiO_3$, I wanted to trace the reactants of the reaction resulting in calcium silicate so Figure 30 represents the mass to charge ratios of CaO and SiO2.

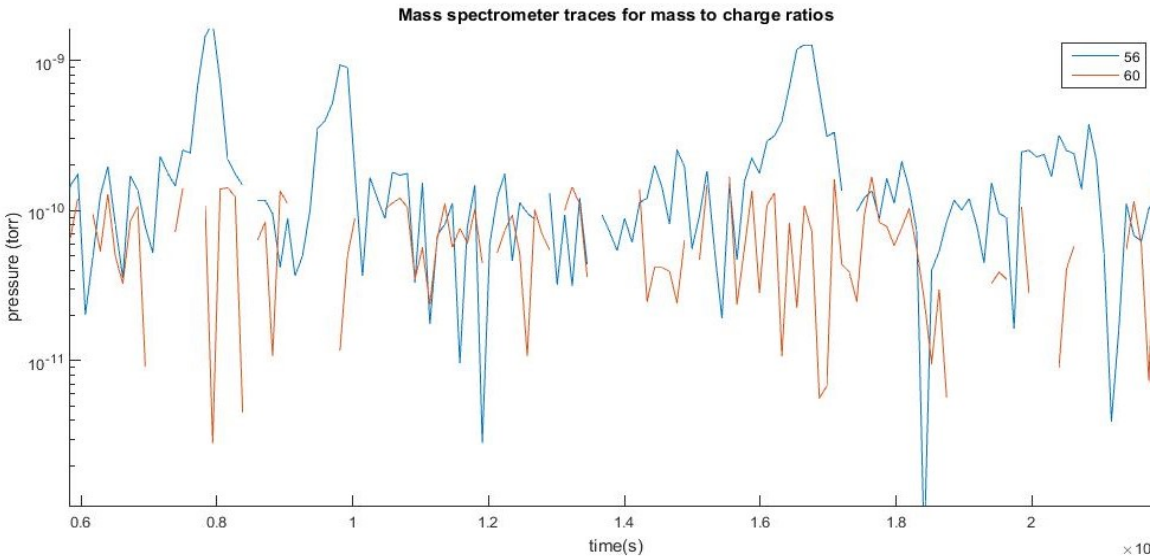

Figure 29. Traces of CaO (blue line, mass/charge: 56) and SiO_2 (red line, mass/charge: 60).

Since the partial pressure of SiO_2 is very low compared to the CaO, the mass spectrometer did not detect it.

Discussion

The first part of the results confirms the identification of AlOSi vapor phase above the melt (amorphous phase) with initial solid state composition of SiO_2 and Al_2O_3 (80/20 molar % composition). My experimental results are compared to Shornikov's work and indicate that the vapor phase composition will be different if the initial material

has a different composition, for example mullite (crystalline Al_2SiO_5, $AlSi_2O_5$, $Al_3Si_2O_{13}$). The experimental infrared spectrum, the Gaussian-calculated infrared spectrum and the mass spectrometer trace all yield the AlOSi radical in the gas phase. In order to confirm my findings, the next experiment should have the mullite initial composition and hopefully it will yield shifted infrared features. Future work should also include a better experimental technique to achieve a 1:1000 ratio of evaporant to Argon – that will prevent the peak shifts and will make the infrared analysis more straightforward.

REFERENCES

Ackerman, S.A., Marley, S.A., 2001, ApJ, 556, 872

Armitage, P.J, 2010, Astrophysics of Planet Formation (Cambridge University Press)

Bailes et al., 2011, Science, 333, 6050, 1717

Batchhelder, D.N., et al., 1967, Phys. Rev., 162, 767

Bondar' V.V., S. I. Lopatin, and V. L. Stolyarova, 2005, Inorganic Materials, 41, 4, 362

Botschwina, P., Rosmus, P., 1985, J. Chem. Phys., 82, No.3, 1421

Charbonneau, D., Brown, T.M., Latham, D.W., et al, 2000, ApJ, 626, 523

Charbonneau, D., et al., 2002, ApJ, 568, 377

Charbonneau, D., 2003, Vol. 294 of ASP Conf. Ser., 449

Charbonneau, D., et al. 2005, ApJ, 626, 523

Clery, D., 2016, Science Mag., AAAS, DOI: 10.1126/science.aag0700

Cruz, K.L., Kirkpatrick, J.D., Burgasser, A.J., 2009, AJ, 354, 1165

Deming, D., et al., 2005, ApJ, 622, 1149

Elkins-Tanton L, Seager S. 2008. Ap. J. 685, 1237

Fortney, J.J. et al. 2007, ApJ, 666, L45-L48

Gaussian 09, Revision A.02, M. J. Frisch, G. W. Trucks, H. B. Schlegel, et al. Gaussian, Inc., Wallingford CT, 2016

Gerasimov, M. V., Yu. P. Dikova, B., O. I. Yakovlev, 2012 Petrology, 20, 5, 399

Greer, S. C., L. Meyer, Z., 1969, Angew. Phys., 27, 198

Hallam, H.E., 1973, Vibrational Spectroscopy of Trapped Species (Wiley)

Henry, G.W., Marcy, G.W., Butler, R.P., et al., 1999, HD 209458, IAU Circ., 7307, 1

Henry, G.W., Marcy, G.W., Butler, R.P., et al., 2000, ApJ, 529, L41-L44

Hidalgo H., 1960. ARS Journal 30:806

Hoch, M., Narasimhamurty, H. V. L., 1963, Final Report, ASD TDR-63-371

Hubbard, W.B., et al., 2001, ApJ, 560, 413

Iosilevskiy, I., Gryaznov, V., Solov'ev, A. 2014, High Temperatures High Pressures 43.2-3, 227

Junker, M., Freisen, M., Schnockel, H., 2000, Journal of Chemical Physics 112, 1444

Kargel, J. S., & Lewis, J. S. 1993, Icarus, 105, 1

Kennard, E.H., 1938, Kinetic Theory of Gases, McGraw-Hill Book Co.

Knutson, H.A., et al., 2008, ApJ, 673, 526

Lang, K.R. 1980, Astrophysical Formulae: a Compendium for the Physicist and Astrophysicist (Springer-Verlag)

Lodders, K., Fegley, B., 2002, Icarus, 155, 2, 393

Lopatin, S. I., S. M. Shugurov, S. M, Stolyarova, V.L., 2008, Dokl. Earth Sci. 418 , 1, 5

Losee, D. L., R. O. Simmons, 1968, Phys. Rev, 172, 944

Mayor M., Queloz D. 1995, Nature 378, 355

Miller-Ricci, E., & Fortney, J. J. 2010, ApJ, 716, L74

Motzfeldt, K., 1955, Method. J. Phys. Chem., 59, 2, 139

Peterson, O.G., 1966 D. N. Batchelder and R. O. Simmons, Phys. Rev, 150, 703

Sahlmann et al., 2013, Astronomy and Astrophysics, 556, A133

Sanchez-Levega, S., Pérez-Hoyos, S., Hueso, R., 2004, American Journal of Physics, 72, 6, 767

Schaefer, L., & Fegley, B., Jr. 2004, Icarus, 169, 216

Schaefer L., Fegley, B. Jr., 2009, ApJ. 703, L113- L117.

Schaefer L, Fegley B Jr., 2010, Icarus 205, 483

Seager, S., and Sasselov D.D., 2000, ApJ, 537, 916

Seager et al. 2007, ApJ, 669, 1279

Seager S, Deming D., 2009. Ap. J. 703, 1884

Sears, D. R., H. P. Klug, 1962, J. Chem. Phys., 37, 3002

Shornikov, S.I., Extended Abstract of Cand. Sci. (Chem.) Dissertation, 1993, St. Petersburg

Shornikov, S.I., Stolyarova, V. L., Shultz, M. M. 1994, Mass Spectr. 8, 5, 478

Shornikov, S. I, Archakov, I. Yu. 2000, Russ. J. Phys. Chem. 74, 5, 684

Shornikov, S. I., Archakov, I. Yu., Chemekova, T. Yu, 2000, Russ. J. Phys. Chem. 74, 5, 677

Shornikov, S.I. and Yakovlev, O.I. Geochem. Int. 2015, 53, 690

Swain, M.R., et al., 2008, Nature, 452, 329

Toomer, G.J., 1984, Ptolemy's Almagest (Springer-Verlag)

Wedepohl, K. H. 1995, Geochim. Cosmochim. Acta, 59, 1217

Winn, N.J., 2010, arXiv: 1001.2010

Wolszczan, A., 1994, Science 264 (5158):538

Whitman, C. I.1952, J. Chem. Phys., 20, 1, 161